AMERICAN ASTRONOMICAL SOCIETY

Making corrections to your proof

Please follow these instructions to mark changes or add notes to your proof. Ensure that you have downloaded the most recent version of Acrobat Reader from **https://get.adobe.com** so you have access to the widest range of annotation tools.

The tools you need to use are contained in **Annotations** in the **Comment** toolbar. You can also right-click on the text for several options. The most useful tools have been highlighted here. If you cannot make the desired change with the tools, please insert a sticky note describing the correction.

Please ensure all changes are visible via the 'Comments List' in the annotated PDF so that your corrections are not missed.

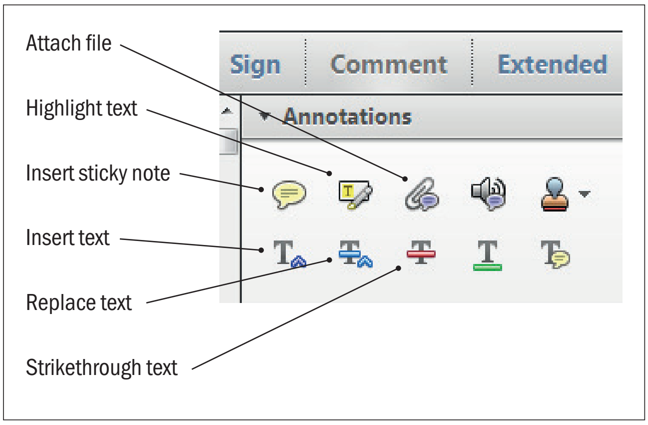

Do not attempt to directly edit the PDF file as changes will not be visible.

Replacing text

To replace text, highlight what you want to change then press the replace text icon, or right-click and press 'Add Note to Replace Text', then insert your text in the pop up box. Highlight the text and right click to style in bold, italic, superscript or subscript.

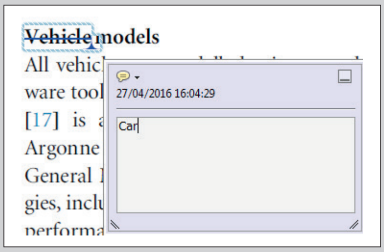

Inserting text

Place your cursor where you want to insert text, then press the insert text icon, or right-click and press 'Insert Text at Cursor', then insert your text in the pop up box. Highlight the text and right click to style in bold, italic, superscript or subscript.

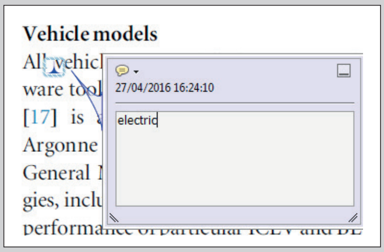

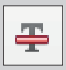

Deleting text

To delete text, highlight what you want to remove then press the strikethrough icon, or right-click and press 'Strikethrough Text'.

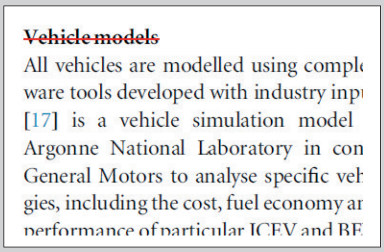

Highlighting text

To highlight text, with the cursor highlight the selected text then press the highlight text icon, or right-click and press 'Highlight text'. If you double click on this highlighted text you can add a comment.

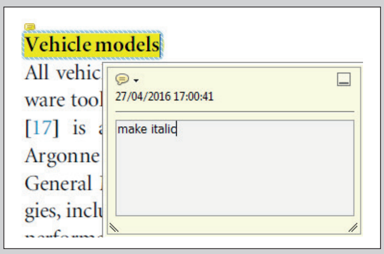

QUERY FORM

JOURNAL: The Astrophysical Journal Supplement Series

AUTHOR: Chilingarian et al.

TITLE: RCSED—A Value-Added Reference Catalog of Spectral Energy Distributions of 800,299 Galaxies in 11 Ultraviolet, Optical, and Near-Infrared Bands: Morphologies, Colors, Ionized Gas, and Stellar Population Properties

ARTICLE ID: apjsaa5462

The layout of this article has not yet been finalized. This proof may contain columns that are not fully balanced/matched or other typographical imperfections; these issues will be resolved once the final corrections have been incorporated.

Please check that the names of all authors as displayed in the proof are correct. Please check also that all authors are linked correctly to the appropriate affiliations.

If you have an Acknowledgments section, please check that the information there is complete and correct.

Page 8

Q1
Please confirm that the edits made to the sentence [Also, there is an important fiber collision effect...] retain the intended sense.

Page 11

Q2
Please provide the initials for the author [Katkov] in reference [Katkov et al. 2016, in preparation].

Page 17

Q3
The URL given in the footnote, http://www.sciops.esa.int/index.php?project=SAT&page=vospec, is not working. Please check and provide a new one as needed.

Page 24

Q4
Please check the details for any journal references that do not have a link; please update with correct details and supply a CrossRef DOI or NASA ADS link if available.

Page 25

Q5
Please provide the publisher details in references [Chilingarian & Katkov 2012, de Vaucouleurs et al. 1991].

APP Template V1.01 Article id: apjsaa5462 Typesetter: MPS Date received by MPS: 08/01/2017 PE: MAC004067 CE : LE:

UNCORRECTED PROOF

The Astrophysical Journal Supplement Series, 00:000000 (25pp), 2017 Month

CrossMark

RCSED—A Value-Added Reference Catalog of Spectral Energy Distributions of 800,299 Galaxies in 11 Ultraviolet, Optical, and Near-Infrared Bands: Morphologies, Colors, Ionized Gas, and Stellar Population Properties*

Igor V. Chilingarian[1,2], Ivan Yu. Zolotukhin[2,3,4], Ivan Yu. Katkov[2], Anne-Laure Melchior[5], Evgeniy V. Rubtsov[2,6], and Kirill A. Grishin[6]

[1] Smithsonian Astrophysical Observatory, 60 Garden St. MS09, Cambridge, MA, 02138, USA; igor.chilingarian@cfa.harvard.edu
[2] Sternberg Astronomical Institute, M.V. Lomonosov Moscow State University, 13 Universitetsky prospect, Moscow, 119991, Russia; ivan.zolotukhin@irap.omp.eu
[3] Université de Toulouse; UPS-OMP, IRAP, 9 avenue du Colonel Roche, BP 44346, F-31028 Toulouse Cedex 4, France
[4] Special Astrophysical Observatory of the Russian AS, Nizhnij Arkhyz 369167, Russia
[5] Sorbonne Universités, UPMC Univ. Paris 6, Observatoire de Paris, PSL Research University, CNRS,UMR F-8112, LERMA, Paris, France
[6] Department of Physics, M.V. Lomonosov Moscow State University, 1, Leninskie Gory, Moscow 119991, Russia
Received 2016 March 21; revised 2016 December 1; accepted 2016 December 6; published 2017 MM DD

Abstract

We present RCSED, the value-added Reference Catalog of Spectral Energy Distributions of galaxies, which contains homogenized spectrophotometric data for 800,299 low- and intermediate-redshift galaxies ($0.007 < z < 0.6$) selected from the Sloan Digital Sky Survey spectroscopic sample. Accessible from the Virtual Observatory (VO) and complemented with detailed information on galaxy properties obtained with state-of-the-art data analysis, RCSED enables direct studies of galaxy formation and evolution over the last 5 Gyr. We provide tabulated color transformations for galaxies of different morphologies and luminosities, and analytic expressions for the red-sequence shape in different colors. RCSED comprises integrated k-corrected photometry in up to 11 ultraviolet, optical, and near-infrared bands published by the *GALEX*, SDSS, and UKIDSS wide-field imaging surveys; results of the stellar population fitting of SDSS spectra including best-fitting templates, velocity dispersions, parameterized star formation histories, and stellar metallicities computed for instantaneous starburst and exponentially declining star formation models; parametric and non-parametric emission line fluxes and profiles; and gas phase metallicities. We link RCSED to the Galaxy Zoo morphological classification and galaxy bulge+disk decomposition results of Simard et al. We construct the color–magnitude, Faber–Jackson, and mass–metallicity relations; compare them with the literature; and discuss systematic errors of the galaxy properties presented in our catalog. RCSED is accessible from the project web site and via VO simple spectrum access and table access services using VO-compliant applications. We describe several examples of SQL queries to the database. Finally, we briefly discuss existing and future scientific applications of RCSED and prospective catalog extensions to higher redshifts and different wavelengths.

Key words: catalogs – galaxies: fundamental parameters – galaxies: photometry – galaxies: stellar content

1. Introduction and Motivation

During the last decade we witnessed a breakthrough in wide-field imaging surveys across the electromagnetic spectrum. The new era started with the Sloan Digital Sky Survey (SDSS), which used a 2.5 m telescope and covered over 11,600 deg^2 of the sky in five optical photometric bands ($ugriz$) down to the 22nd AB magnitude in its latest seventh legacy data release (Abazajian et al. 2009). It had a spectroscopic follow-up survey that targeted over 1 million galaxies and quasars and half a million stars down to the magnitude limit of $r = 17.77$ AB mag. Even though by the end of 2015 the data from SDSS and its successors, SDSS-II and SDSS-III, have been used in about 20,000 research papers,[7] the SDSS potential for scientific exploration remains far from exhausted.

In the late 2000s, deep wide-field surveys went beyond the optical spectral domain. The *Galaxy Evolution Explorer* (*GALEX*) satellite (Martin et al. 2005) provided nearly all-sky photometric coverage in two ultraviolet bands centered at 154 and 228 nm down to the limiting magnitudes $AB = 20.5$ mag. The SDSS footprint area was observed by *GALEX* with a 15 times longer exposure that yielded a much deeper limit of $AB = 23.5$ mag. The relatively small telescope provided the spatial resolution of a couple of arcseconds comparable to the typical image quality level at ground-based facilities.

At the same time, a major effort was undertaken by the international team at the 4 m United Kingdom Infrared Telescope UKIRT to survey a substantial area of the sky largely overlapping with the SDSS footprint in four near-infrared (NIR) bands ($YJHK$). The Large Area Survey of the UKIRT Deep Sky Survey (UKIDSS LAS; Lawrence et al. 2007) provides sub-arcsecond resolution and flux limit comparable to that of SDSS in the optical domain. It reaches $AB \sim 21.2$ mag, 3–4 mag deeper than the first all-sky NIR survey, 2MASS (Skrutskie et al. 2006).

Numerous projects studied the entire SDSS spectroscopic sample of galaxies by analyzing both absorption (see e.g., Kauffmann et al. 2003; Gallazzi et al. 2006) and emission lines (Brinchmann et al. 2004; Tremonti et al. 2004; Oh et al. 2011, 2015) in SDSS spectra (MPA-JHU and OSSY catalogs). However, they did not make use of any additional information beyond that available in the SDSS database.

The first successful attempt of providing an added value to SDSS data was done a decade ago in the "New York University Value-Added Galaxy Catalog" (NYU-VAGC)

* The data tables and other supporting technical information are available at the project website: http://rcsed.sai.msu.ru/.
[7] According to NASA ADS, http://ads.harvard.edu/.

project (Blanton et al. 2005). It was aimed at statistical studies of galaxy properties and the large-scale structure of the universe, and included a compilation of information derived from photometry and spectroscopy in one of the earlier SDSS data releases (which represents about 20% of its final imaging footprint). It also comprised positional cross-matches with 2MASS, far-infrared *IRAS* point-source catalog (Saunders et al. 2000), the Faint Images of the Radio sky 20 cm survey, FIRST (Becker et al. 1995), and additional data on galaxies from the Third Reference Catalog of Bright Galaxies (de Vaucouleurs et al. 1991) and the Two-Degree Field Galaxy Redshift Survey (Colless et al. 2001). Now, a decade after NYU-VAGC has been published, there is a sharp need to assemble a next generation of a value-added galaxy catalog based on modern survey data that were not available back then.

Here we present a new generation and different flavor of a value-added catalog of galaxies based on a combination of data from the SDSS, *GALEX*, and UKIDSS surveys that also includes comprehensive analysis of absorption and emission lines in galaxy spectra. Our main motivation is to use the synergy provided by the joint panchromatic data set for extragalactic astrophysics: the optical domain is traditionally the best studied and there exist well-calibrated stellar population models; the UV fluxes are sensitive to even small fractions of recently formed stars and therefore contain valuable information on star formation histories; the near-IR band is substantially less sensitive to the internal dust reddening and stellar population ages, and therefore can provide good stellar mass estimates. Our mission is to build a reference multi-wavelength spectrophotometric data set and complement it with additional detailed information on galaxy properties so that it will allow astronomers to study galaxy formation and evolution at redshifts $z = 0.0$–0.6 in a transparent way with as few extra manipulations as possible.

We aim to provide (i) the first homogeneous set of low-redshift galaxy FUV-to-NIR spectral energy distributions (SEDs) corrected to rest frame for hundreds of thousands of objects, (ii) the first photometric data set containing rest-frame aperture SEDs with corresponding spectra and their stellar population analysis: velocity dispersions, parameterized star formation histories, (iii) consistent analysis of absorption and emission lines in SDSS galaxy spectra including parametric and nonparametric emission line fitting performed using state-of-the-art stellar population models, which cover a wider range of ages and metallicities and, therefore, help to minimize the template mismatch, (iv) easy and fully Virtual Observatory compliant data access mechanisms for our data set and several third-party catalogs that include morphological and structural information for galaxies in our sample.

We started this project in 2009 by developing a new approach to convert galaxy SEDs to the rest frame by calculating analytic approximations of k-corrections in the optical and NIR bands (Chilingarian et al. 2010). Then we extended our algorithm to *GALEX* FUV and NUV bands and discovered a universal three-dimensional relation of NUV and optical galaxy colors and luminosities (Chilingarian & Zolotukhin 2012). Then, we fitted SDSS spectra using state-of-the-art stellar population models, derived velocity dispersions and stellar ages and metallicities, and provided our measurements to the project that calibrated the fundamental plane of galaxies (Djorgovski & Davis 1987) in SDSS by vigorous statistical analysis (Saulder et al. 2013). Our data set also helped find and characterize massive compact early-type galaxies at intermediate redshifts (Damjanov et al. 2013, 2014). Finally, we used a complex set of selection criteria and discovered a large sample of previously considered extremely rare compact elliptical galaxies (Chilingarian & Zolotukhin 2015).

The paper is organized as follows: in Section 2 we describe the construction of the catalog, which includes cross-matching of the three surveys, adding third-party catalogs, and absorption and emission line analysis of SDSS spectra; in Section 3 we discuss the photometric properties of the sample and derive mean colors of galaxies of different morphological types across the spectrum; in Section 4 we explore the information derived from our spectral analysis; Section 5 contains the description of the catalog access interfaces; Section 6 provides the summary of our project; and the Appendices include some technical details on the catalog construction, a detailed description of tables included in the database, and discussion of systematic uncertainties of emission line measurements.

2. Construction of the Catalog

2.1. The Input Sample and Data Sources Used

We compiled the photometric catalog by reprocessing several publicly available data sets. Our core object list is the SDSS Data Release 7 (Abazajian et al. 2009) spectral sample of non-active galaxies (marked as "GAL_EM" or "GALAXY" specclass in the SDSS database) in the redshift range $0.007 \leqslant z < 0.6$. We provide the exact query that we used to select this sample in the SDSS CasJobs Data System[8] in Appendix B. The query executed in the DR7 CasJobs context returned 800,299 records. We deliberately excluded quasars and Seyfert-1 galaxies (specclass = "QSO") because neither the k-correction technique nor stellar population analysis algorithm supported that object type. We used the output table as an input list for positional cross-matches against *GALEX* Data Release 6 (Martin et al. 2005) and UKIDSS Data Release 10 (Lawrence et al. 2007).

For the UKIDSS cross-match we queried the UKIDSS Large Area Survey catalog using the best match criterion within a 3 arcsec radius. In order to perform this query, we employed the WFCAM Science Archive[9] for programmatic access to the International Virtual Observatory Alliance (IVOA) ConeSearch service with a multiple cone search ("multi-cone") capability. The query returned 280,870 UKIDSS objects matching the galaxies from our input sample. We used the STILTS software package (Taylor 2006) in order to access the UKIDSS data and merge the tables.

Then we uploaded the input SDSS galaxy list to the *GALEX* CasJobs web interface[10] and searched for best matches within 3 arcsec, similarly to the UKIDSS cross-match. The query returned 485,996 *GALEX* objects.

As a result of this selection procedure, we compiled an input catalog of 800,299 spectroscopically confirmed SDSS galaxies, out of which 90,717 have eleven-band photometry (two *GALEX* FUV and *NUV*, five *SDSS ugriz* bands, four UKIDSS *YJHK* bands); 163,709 have all UKIDSS bands and at least one UV band; and 582,534 have at least one additional photometric band to SDSS bands. In Figure 1 we present the

[8] http://skyserver.sdss3.org/CasJobs/
[9] http://surveys.roe.ac.uk/wsa/
[10] http://galex.stsci.edu/casjobs/

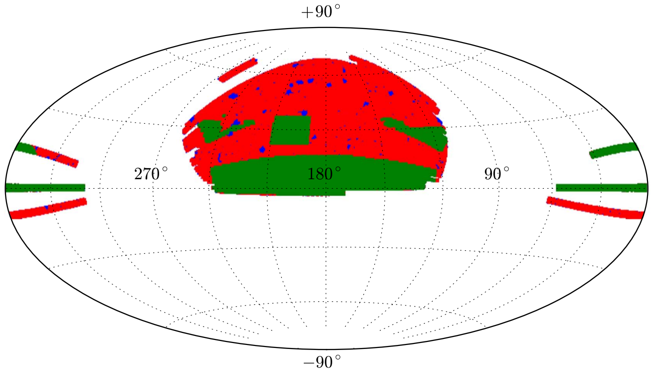

Figure 1. A full-sky Aitoff projection in equatorial coordinates demonstrating the footprint of our catalog. Green areas denote the availability of all three input photometric data sets: SDSS, UKIDSS, and *GALEX*; red areas are for SDSS and *GALEX*; and blue areas are for SDSS only. Note that we include all objects from the input data sets that have at least one flux measurement in them.

Table 1
Number of Objects in the Combined Sample with Photometric Measurements Available from Three Input Photometric Catalogs

Photometric Bands	Number of Galaxies
SDSS *ugriz*	799783
GALEX FUV + *ugriz*	286570
GALEX NUV + *ugriz*	469419
FUV + NUV + *ugriz*	270152
ugriz + UKIDSS *Y*	270603
ugriz + UKIDSS *J*	265316
ugriz + UKIDSS *H*	272028
ugriz + UKIDSS *K*	273050
ugriz + *Y JHK*	250608
NUV + *ugriz* + *Y JHK*	157531
All 11 bands	90717

footprint of our catalog on the all-sky Aitoff projection marking the regions covered by all three wide field imaging surveys using different colors. The statistics of galaxies measured in different photometric bands is given in Table 1.

Then we linked the following published data sets to our catalog in order to contribute the spectrophotometric information to some of the most widely used galaxy properties: (i) the results of the two-dimensional light profile decomposition of SDSS galaxies by Simard et al. (2011) that include structural properties of all objects in our catalog; (ii) the morphological classification table from the citizen science "Galaxy Zoo" project (Lintott et al. 2008, 2011) that provides a human eye classification of well spatially resolved SDSS galaxies made by citizen scientists. In our sample, 661,319 objects have 10 or more morphological classifications in the Galaxy Zoo catalog (*nvote* $\geqslant 10$).

2.2. The Photometric Catalog

2.2.1. Petrosian and Aperture Magnitudes

All three photometric surveys used in our study provide extended source photometry along with aperture measurements made in several different aperture sizes (*GALEX* and UKIDSS).

For the SED photometric analysis and construction of scaling relations involving galaxy luminosity, we need total magnitudes. For this purpose we adopt Petrosian (1976) magnitudes available in SDSS and UKIDSS as measurements

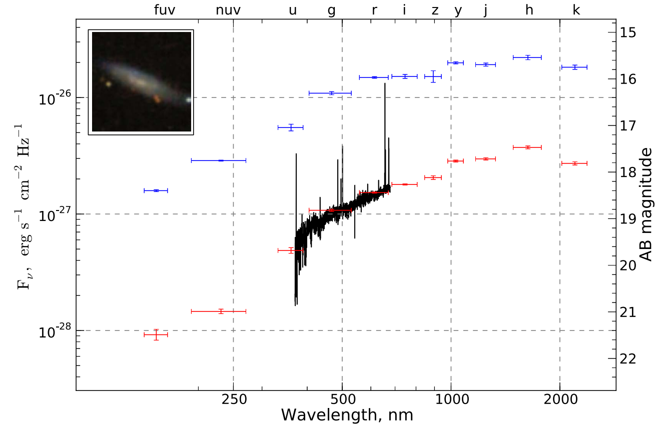

Figure 2. Example of fully corrected SED in 11 bands for a late-type spiral galaxy at redshift 0.035. Blue and red symbols represent total (Petrosian) and 3 arcsec fiber magnitudes, respectively. The rest-frame SDSS spectrum is overplotted and demonstrates typical excellent agreement with the corrected fiber magnitudes for that galaxy. The inset shows a 36 × 36 arcsec optical SDSS false-color image.

that do not significantly depend on galaxy light profile shapes conversely to SDSS *modelmags* (see discussion in Chilingarian & Zolotukhin 2012). The *GALEX* catalog provides "total" magnitudes that are close to Petrosian magnitudes for exponential surface brightness profiles (i.e., disk galaxies) and up to 0.2 mag brighter for elliptical galaxies (Yasuda et al. 2001). However, given the average photometric uncertainty in the *GALEX* NUV fluxes of red galaxies of 0.3 mag, we can neglect this difference.

On the other hand, our parent sample of galaxies was derived from the SDSS spectroscopic sample, and all SDSS DR7 spectra were obtained in circular 3 arcsec-wide apertures. Therefore, we need 3 arcsec aperture magnitudes in order to make quantitative comparison of spectroscopic and photometric data. Hence, we computed aperture magnitudes for all *GALEX* and UKIDSS sources with available aperture measurements by interpolating the flux to a 3 arcsec aperture, and used SDSS *fibermags* for the optical SED part. Note that the spatial resolution of the *GALEX* survey in the NUV band is about 5 arcsec; therefore, 3 arcsec aperture magnitudes will be slightly underestimated for small objects. For compact (point-like) sources, a 3 arcsec aperture NUV magnitude can be underestimated by as much as 0.3 mag; however, such objects are very rare in the SDSS DR7 galaxy sample. Damjanov et al. (2013) and Zahid et al. (2015, 2016) found a couple of thousands of compact sources in SDSS and SDSS-III BOSS, only a few hundred of which were in SDSS DR7. We estimated the number of compact galaxies in our sample by selecting the sources where the average difference of aperture and Petrosian magnitudes in the *ugriz* bands was <0.3 mag: this query returned 831 objects or <0.1% of the sample.

We corrected the obtained sets of Petrosian and 3 arcsec aperture magnitudes for the Galactic foreground extinction by using the $E(B-V)$ values computed from the Schlegel et al. (1998) extinction maps. Then, we computed *k*-corrections for both sets of photometric points using the analytic approximations presented in Chilingarian et al. (2010) and updated for *GALEX* bands in Chilingarian & Zolotukhin (2012).

In Figure 2 we provide an example of a fully corrected SED for a late-type spiral galaxy ($z = 0.035$) that has flux measurements in all 11 bands. We show both total and fiber magnitudes and overplot an SDSS spectrum with the wavelength axis converted into the rest frame and fluxes converted into *AB* magnitudes. One can see a remarkable agreement between the corrected photometric points and the observed spectral flux density, typical for our catalog.

2.2.2. Correcting the SDSS–UKIDSS Photometric Offset

An important problem of the UKIDSS photometric catalog of extended sources is the observed spread of colors including optical SDSS and NIR UKIDSS photometric measurements (e.g., $g - J$ for red sequence galaxies). We detected this inconsistency in Chilingarian et al. (2010) and applied an empirical correction to UKIDSS magnitudes based on the assumption of continuous SEDs of galaxies. We computed $z - Y$ colors by interpolating over all other available colors, approximating the SED with a low-order polynomial function. This approach, however, required the availability of the *Y*-band photometry in the UKIDSS catalog. We have analyzed the SDSS–UKIDSS Petrosian magnitude offset amplitude for different galaxies and concluded that it originates from the surface brightness limitation imposed by the relatively short integration time in UKIDSS and by the high and variable sky background level in the NIR. Therefore, Petrosian radii and magnitudes become underestimated, and comparison of original UKIDSS extended source magnitudes with SDSS and *GALEX* integrated photometry becomes impossible, because any color including data from UKIDSS and another data source depends on the galaxy surface brightness and size.

Here we propose a general and simple empirical solution. We exploit the UKIDSS Galactic Cluster Survey photometric catalog, which includes *Z*-band photometry, convert it into SDSS *z* with the available color transformation (Hewett et al. 2006) for both Petrosian and 3 arcsec aperture magnitudes, and compare it to actual SDSS *z*-band measurements from the SDSS DR7 catalog for exactly the same objects. It turns out that (i) the Petrosian magnitude difference $z_{\rm SDSS,Petro}$ $z_{\rm UKIDSS,Petro}$ correlates with the galaxy mean surface brightness, (ii) the fiber magnitude difference $z_{\rm SDSS,fib} - z_{\rm UKIDSS,3''}$ is close to zero within 0.02 mag, and (iii) differences between Petrosian and fiber magnitudes in all UKIDSS photometric bands (*ZYJHK*) are almost identical, which indicates virtually flat NIR color profiles in most galaxies. This suggests that the correction for UKIDSS Petrosian magnitudes should be calculated as $\Delta(mag_{\rm UKIDSS,Petro}) = (z_{\rm SDSS,fib}\ z_{\rm SDSS,Petro})\ (Y_{\rm UKIDSS,3''} - Y_{\rm UKIDSS,Petro})$. This transformation adjusts the UKIDSS integrated photometry in a way that the differences between the 3 arcsec and Petrosian magnitudes of a galaxy in the *z* and *Y* bands become equal. For objects, where *Y* magnitudes are not available in the UKIDSS survey, we use the next available photometric band (*J*, *H*, or *K*).

In this fashion, we obtained fully corrected FUV-to-NIR spectral energy distributions converted into rest-frame magnitudes for a large sample of galaxies in 3 arcsec apertures and integrated over entire galaxies.

2.3. The Spectral Catalog: Absorption Lines

We fitted all SDSS spectra using the NBURSTS full spectrum fitting technique (Chilingarian et al. 2007a, 2007b) and determined their radial velocities v, stellar velocity dispersions σ, and parameterized star formation histories represented by an instantaneous star burst (simple stellar populations, SSP) or an exponentially declining star formation history (exp-SFH), assuming that it started shortly after the big bang. We chose these two families of stellar population models because, (i) SSP models are widely used in extragalactic studies by different authors and we wanted our data to be directly comparable to other sources and (ii) exponentially declining SFHs were demonstrated to be a better representation of broadband SEDs of non-active galaxies (Chilingarian & Zolotukhin 2012) than SSPs. We should, however, note that exp-SFH models cannot adequately describe young stellar populations with mean ages $t < 1.5$ Gyr (see discussion below).

The fitting procedure first convolves a grid of stellar population models with the wavelength-dependent spectral line spread function available for every SDSS spectrum in the original data files, then runs a nonlinear Levenberg–Markquardt minimization by first choosing a model spectrum from the grid by two-dimensional interpolation in the age–metallicity (t–[Fe/H]) space, then convolving it with a Gaussian–Hermite representation of the line-of-sight velocity distribution (LOSVD) of stars in a galaxy described by v, σ, $h3$, $h4$, and finally multiplying it by a low-order Legendre polynomial continuum (its parameters are determined linearly in a separate loop) in order to absorb flux calibration imperfections and possible internal extinction in a galaxy. Hence, the procedure returns values of v, σ, $h3$, $h4$, t, [Fe/H], and coefficients of the multiplicative polynomial continuum. Here we use a pure Gaussian LOSVD shape with $h3 = h4 = 0$.

The NBURSTS algorithm is similar to the penalized pixel-fitting approach by Cappellari & Emsellem (2004). It, however, has some important differences. (i) We use a linear fit of the low-order multiplicative polynomial continuum because its parameters are decoupled from galaxy kinematics and stellar populations. (ii) Instead of using a fixed grid of template spectra and interpreting stellar populations using their relative weights in a linear combination, we interpolate in a grid of models inside the minimization loop in order to obtain the best-fitting stellar population parameters of each starburst (or an exponentially declining model). As a result, for the simplest case of a single-component SSP model, we obtain the best-fitting SSP-equivalent age and metallicity. These values are usually close to the luminosity-weighted ones; however, in cases of complex SFHs approximated by an SSP, there might be biases similar to those affecting Lick indices (Serra & Trager 2007). Chilingarian et al. (2007b, 2008) demonstrated that SSP equivalent ages and metallicity remain unbiased for galaxies with super-solar α-element abundances ([Mg/Fe] > 0 dex) and when Balmer line regions are masked in order to fit emission lines.

We excluded the spectral regions affected by bright atmosphere lines (O I, NaD, OH, etc.) and by the *A* and *B* telluric absorption bands from the fitting procedure. We also re-ran the fitting code excluding 8–14 Å wide regions around locations of bright emission lines for objects, where the reduced χ^2 value of the fit exceeded the threshold $\chi^2/\mathrm{DOF} = 0.8$, that were selected empirically from a sample of galaxies without and with emission lines of different intensity levels.[11]

We used three grids of stellar population models, all computed with the PEGASE.HR evolutionary synthesis code (Le Borgne et al. 2004):

[11] Published SDSS spectra are slightly oversampled in wavelength; therefore, flux uncertainties in neighboring pixels are correlated and, hence, the reduced χ^2 for a spectrum well represented by its model is less than 1 (around 0.6).

1. SSP models based on the high-resolution ($R = 10000$) ELODIE.3.1 empirical stellar library (Prugniel & Soubiran 2004; Prugniel et al. 2007) covering the wavelength range $3900 < \lambda < 6800$ Å, the metallicity range $-2.5 <$ [Fe/H] < 0.5 dex, and ages $20 < t < 20{,}000$ Myr.
2. Models with exponentially declining SFH at a constant metallicity computed for the same metallicity and wavelength ranges as those for SSP models, covering the range of exponential decay timescales $10 < \tau < 20{,}600$ Myr (the latter one effectively being a constant star-formation rate model) and starting epochs of star formation between 4.3 Gyr and 13.8 Gyr of the age of the universe corresponding to the redshift range $0 < z < 1.5$. We used the exponential decay timescale τ in the same fashion as the SSP age in the minimization procedure. For every galaxy, we first computed a grid of τ−[Fe/H] models with the star-formation epoch corresponding to its redshift, assuming that a galaxy was formed at very high redshift, e.g., for $z = 0.2$ with the light travel time of 45 Gyr, we computed a grid of models for star formation that started 11.27 Gyr ago, assuming standard WMAP9 cosmology (Hinshaw et al. 2013).
3. Intermediate-resolution SSP models ($R = 2300$) based on the MILES empirical stellar library (Sánchez-Blázquez et al. 2006) covering the wavelength range $3600 < \lambda < 7400$ Å, the metallicity range $-2.5 <$ [Fe/H] < 0.7 dex, and ages $20 < t < 20{,}000$ Myr.

We stress that the best-fitting stellar population ages $t > 14{,}000$ Myr (SSP) and exponential timescales $\tau < 1000$ Myr (exp-SFH) should be considered as upper and lower limits for the corresponding parameters.

In the public version of our catalog we provide two sets of stellar population parameters for every galaxy: (1) SSP ages and metallicities obtained from the spectrum fitting in the wavelength range in a galaxy rest frame $4500 < \lambda < 6795$ Å using the MILES- PEGASE.HR models with the fifth degree of the multiplicative polynomial continuum and (2) PEGASE.HR-based exponentially declining SFR models in the wavelength range $3915 < \lambda < 6795$ Å with the 19th degree continuum. The 19th degree corresponds to the emipirically determined optimal degree of the multiplicative polynomial continuum for SDSS spectra when the χ^2 value reaches a "plateau" as explained in Chilingarian et al. (2008). We performed the SSP fitting with the MILES- PEGASE.HR models in the truncated wavelength range with a very low-order polynomial continuum in order to minimize the artifacts originating from imperfections in the SSP model grid (see Section 4.2). In the publicly available Simple Spectrum Access Service, we provide the results of the MILES- PEGASE.HR-based SSP fitting in the wavelength range $3600 < \lambda < 6790$ Å in order to enable emission line analysis from the fitting residuals for all lines including the [O II] 3727 Å doublet.

2.4. The Spectral Catalog: Emission Lines

Our full spectral fitting procedure precisely matches the stellar continuum of each galaxy with the best-fitting stellar population model (see example in Figure 3). Although the regions of all Balmer absorption lines are age sensitive, they contain at most 20% of the age-sensitive information from the entire optical spectral range (Chilingarian 2009). Chilingarian et al. (2007b) have demonstrated that masking the Hβ and Hγ regions biases neither age nor metallicity determinations by the NBURSTS procedure. Hence, we do not expect to introduce significant template mismatch by masking the regions of emission lines when fitting SDSS spectra. Having subtracted the best-fitting model, we obtain clean emission line spectra unaffected by stellar absorptions that is especially important for the Balmer lines. The precision of our stellar continuum fitting allows us to recover faint emission lines at a few percent level of the continuum intensity, whereas very often such lines are not detected in the SDSS spectral pipeline results. In Table 2 we provide the statistics of the emission line detection and strength in our sample.

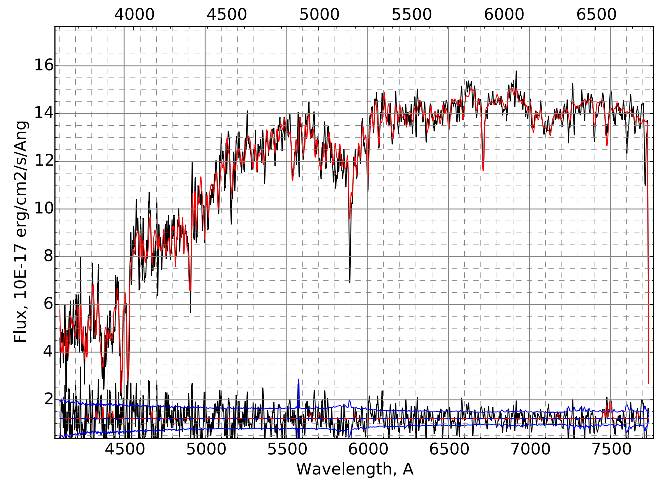

Figure 3. Example of the NBURSTS full spectrum fitting for an SDSS spectrum of an early-type galaxy. An observed galaxy spectrum is shown in black, the best-fitting template is in red, residuals are in blue. Regions of emission lines excluded from the fitting are shown red in the residuals. The observed and rest-frame wavelengths are shown in the bottom and top of the plot, respectively.

In order to measure the fluxes and equivalent widths (EW) of emission lines, we used two different approaches, namely, Gaussian and non-parametric fitting of emission line profiles.

In some galaxies, emission line profiles cannot be described by a Gaussian. This is often the case in galaxies with peculiar gas kinematics, e.g., multicomponent bulk gas motions and outflows can produce complex asymmetric lines. Also, this is crucially important for active galactic nuclei (AGNs) with broad components in Balmer lines. Approximation of such emission lines by a Gaussian profile results in biased estimates of flux and kinematic parameters. We address this problem by employing a non-parametric fitting approach, which allows us to recover arbitrary line profiles and measure their fluxes with higher precision. At the same time, this method requires several lines with sufficiently high S/N to be present in a spectrum, and may produce biased results when dealing with noisy data. We, therefore, perform a "classical" Gaussian profile fitting too in order to allow for cross-comparison and validation of our line fitting results.

Both non-parametric and Gaussian fitting techniques take into account the SDSS line spread function computed individually for each spectrum by the standard SDSS pipeline and provided in FITS (Flexible Image Transport System) tables in the RCSED distribution.

2.4.1. Gaussian Fitting

This approach consists of simultaneously fitting the entire set of emission lines (see the line list in Table 2) with Gaussians

Table 2
Emission Line Detection Statistics (the Parametric Gaussian Fit) at Different Signal-to-noise Ratios (S/N)

Line	Wavelength Å	Prefix	Covered N	S/N > 1 N	S/N > 1 fraction	S/N > 3 N	S/N > 3 fraction	S/N > 5 N	S/N > 5 fraction	S/N > 10 N	S/N > 10 fraction
[O II]	3726.03	f3727_oii	780665	543374	69.6%	354307	45.4%	225669	28.9%	92161	11.81%
[O II]	3728.82	f3730_oii	782417	562707	71.9%	387264	49.5%	257713	32.9%	110287	14.10%
Hκ	3750.15	f3751_h_kappa	791720	233850	29.5%	26219	3.3%	5584	0.7%	535	0.07%
Hι	3770.63	f3772_h_iota	796081	180306	22.6%	18912	2.4%	4524	0.6%	595	0.07%
Hθ	3797.90	f3799_h_theta	798386	229961	28.8%	31590	4.0%	8466	1.1%	1345	0.17%
Hη	3835.38	f3836_h_eta	798565	255213	32.0%	52680	6.6%	16876	2.1%	2976	0.37%
[Ne III]	3868.76	f3870_neiii	798635	246202	30.8%	45733	5.7%	19500	2.4%	7579	0.95%
He I	3887.90	f3889_hei	798674	182764	22.9%	37166	4.7%	10644	1.3%	1328	0.17%
Hζ	3889.07	f3890_h_zeta	798675	223107	27.9%	63940	8.0%	26166	3.3%	6072	0.76%
Hϵ	3970.08	f3971_h_epsilon	798835	360759	45.2%	156226	19.6%	78430	9.8%	21312	2.67%
[S II]	4068.60	f4070_sii	799003	202235	25.3%	14766	1.8%	2352	0.3%	149	0.02%
[S II]	4076.35	f4078_sii	799010	149342	18.7%	4755	0.6%	517	0.1%	55	0.01%
Hδ	4101.73	f4103_h_delta	799043	342858	42.9%	172913	21.6%	96748	12.1%	32463	4.06%
Hγ	4340.46	f4342_h_gamma	799276	419668	52.5%	275775	34.5%	192540	24.1%	87637	10.96%
[O III]	4363.21	f4364_oiii	799293	118667	14.8%	8001	1.0%	2569	0.3%	787	0.10%
He II	4685.76	f4687_heii	799381	109369	13.7%	6779	0.8%	2204	0.3%	614	0.08%
[Ar IV]	4711.37	f4713_ariv	799381	79310	9.9%	3477	0.4%	530	0.1%	110	0.01%
[Ar IV]	4740.17	f4742_ariv	799380	118077	14.8%	7031	0.9%	1108	0.1%	85	0.01%
Hβ	4861.36	f4863_h_beta	799375	514321	64.3%	381556	47.7%	317350	39.7%	214953	26.89%
[O III]	4958.91	f4960_oiii	799372	449021	56.2%	164285	20.6%	92442	11.6%	47287	5.92%
[O III]	5006.84	f5008_oiii	799371	638852	79.9%	404135	50.6%	244845	30.6%	119215	14.91%
[N I]	5197.90	f5199_ni	799360	144430	18.1%	9742	1.2%	1345	0.2%	178	0.02%
[N I]	5200.25	f5202_ni	799360	184255	23.1%	16318	2.0%	2676	0.3%	226	0.03%
[N II]	5754.59	f5756_nii	799131	196670	24.6%	12800	1.6%	2763	0.3%	966	0.12%
He I	5875.62	f5877_hei	798546	260312	32.6%	81904	10.3%	38829	4.9%	12209	1.53%
[O I]	6300.30	f6302_oi	784763	439640	56.0%	177144	22.6%	77850	9.9%	16856	2.15%
[O I]	6363.78	f6366_oi	780219	285886	36.6%	40626	5.2%	9143	1.2%	1395	0.18%
[N II]	6548.05	f6550_nii	764832	596254	78.0%	422810	55.3%	289961	37.9%	133553	17.46%
Hα	6562.79	f6565_h_alpha	763451	614029	80.4%	531966	69.7%	479842	62.9%	395722	51.83%
[N II]	6583.45	f6585_nii	761376	641883	84.3%	553212	72.7%	479386	63.0%	334901	43.99%
He I	6678.15	f6679_hei	750612	178330	23.8%	21069	2.8%	6321	0.8%	1408	0.19%
[S II]	6716.43	f6718_sii	745687	571758	76.7%	423064	56.7%	320126	42.9%	186973	25.07%
[S II]	6730.81	f6733_sii	743742	554071	74.5%	374143	50.3%	263155	35.4%	135572	18.23%

Notes. The "covered" column reflects the number of objects with a corresponding line in the wavelength coverage. The "wavelength" column provides air wavelengths. The "prefix" column gives the prefix of the column names for the corresponding spectral line in the emission line fits tables from the rcsed distribution.

pre-convolved with the SDSS line spread function. We allow two different sets of redshifts and intrinsic widths for the recombination and forbidden lines. We estimate the kinematic parameters with the nonlinear least-squares minimization that is implemented by the MPFIT package[12] (Markwardt 2009). The emission line fluxes are computed linearly for each minimization iteration. When solving the linear problem, we constrain the line fluxes to be non-negative. For this purpose we use the BVLS (bounded-variables least-squares) algorithm (Lawson & Hanson 1995) and its implementation by M. Cappellari.[13]

2.4.2. Non-parametric Emission Line Fitting

Our non-parametric emission line fitting method includes two main steps, which we repeat several times until convergence is achieved. First, we derive discretely sampled emission line profiles, i.e., line-of-sight velocity distributions (LOSVDs) of ionized gas. During the second step, we estimate emission line fluxes. Because allowed and forbidden transitions often originate from different regions of a galaxy having very different physical properties (i.e., density, temperature, mechanism of excitation), although all emission lines of each type (allowed and forbidden) have similar shapes, our procedure recovers two different non-parametric profiles, one for each type.

The LOSVD derivation is organized as follows. We note that convolution of any logarithmically rebinned observed spectrum $S_{\rm obs}$ of m elements with LOSVD $\mathcal{L}$ having n elements can be expressed as a linear matrix equation $A * \mathcal{L} = S_{\rm obs}$, where A is an $m \times n$ matrix of template spectra having lengths of m pixels each. Every template spectrum from the ith row in the matrix A is shifted by the velocity, which represents the ith position within the LOSVD vector. Here a template spectrum is a synthetic spectrum made of a set of flux-normalized Gaussians with LSF widths representing emission lines detected in the observed spectrum. Such approach allows us to take into account the SDSS instrumental resolution instead of a set of Dirac δ functions. The continuum level of a template spectrum is set to zero.

Thus, we end up with a linear inverse problem whose solution $\mathcal{L}$ can be derived by a least-squares technique. The emission line profiles obviously cannot be negative and, therefore, we use the BVLS algorithm mentioned above.

Once the LOSVD has been derived, we compute the emission line fluxes by solving a linear problem similar to that described in Section 2.4.1. This finishes the first iteration.

[12] http://www.physics.wisc.edu/~craigm/idl/fitting.html
[13] http://www-astro.physics.ox.ac.uk/~mxc/software/bvls.pro

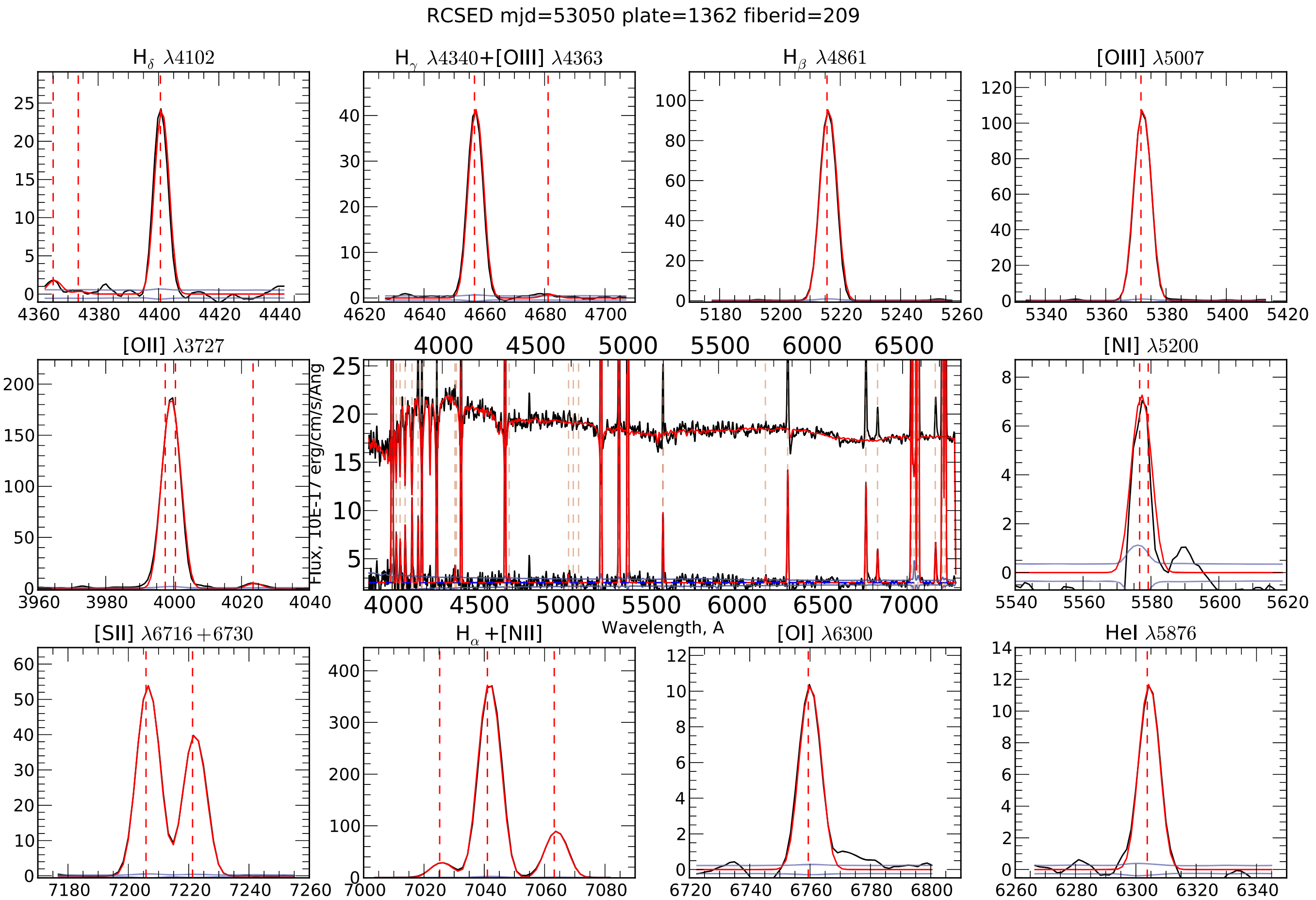

Figure 4. Example of the NBURSTS full spectrum fitting for an SDSS spectrum of a late-type galaxy together with the emission line fitting. The central panel is similar to Figure 3; panels on the sides demonstrate recovered profiles after the continuum subtraction of individual emission lines (black) and the best-fitting models (red). Blue lines show emission line flux uncertainties. Vertical red dashed lines represent the galaxy redshift in the SDSS database.

At the same time, the LOSVD derivation step requires the knowledge of emission line fluxes in order to construct better template spectra. During the first iteration when they are unknown, we set all fluxes to unity and ~~the all-template~~ spectra hence are made of equally normalized Gaussians. Typically, three iterations of this procedure are enough to reach the convergence.

A linear inversion is an ill-conditioned problem and is sensitive to noise in the data. In order to improve the profile reconstruction quality, we exploit a regularization technique, which minimizes the squared third derivative of the recovered line profile. This approach, however, causes artifacts in the sharp narrow-line profiles. Therefore, we apply the regularization only in the wings of emission lines where flux levels are generally low and, consequently, noise is higher. The regularization technique yields the dramatic improvement of recovered Balmer line profiles for faint AGNs. In the catalog we provide measurements of non-parametric emission lines with and without regularization.

The comparison between the parametric (Gaussian) and non-parametric fitting results for a complex emission line profile in a Seyfert galaxy is presented in Figure 5. A Gaussian approximation for such lines is often inadequate and causes serious biases in the kinematics that can reach a few hundred km s^{-1}.

We ran Monte Carlo simulations for a random sample of 2000 objects with emission lines of different intensity levels in order to estimate realistic flux uncertainties obtained with the non-parametric fitting technique. They turned out to be consistent with statistical uncertainties of Gaussian emission line fluxes for most objects and up to a factor of 2 lower for AGNs with broadline components. The RCSED database will be updated with Monte Carlo based uncertainties as we compute them: this procedure is very computationally intensive and will take a couple of months to complete.

2.4.3. Gas Phase Metallicities

We used our emission line flux measurements in order to estimate the gas phase metallicities for galaxies where emissions originate from the ~~star formation-induced~~ excitation. We exploited two different techniques to measure the metallicity, (i) a new calibration by Dopita et al. (2016) and (ii) the IZI Bayesian technique (Blanc et al. 2015) using a grid of models ($\kappa = \infty$) with κ-distributed electron energies (Dopita et al. 2013). We selected ~~star formation-dominated~~ and "transition type" galaxies using the standard BPT (Baldwin et al. 1981) diagram that exploits hydrogen, nitrogen, and oxygen emission lines with the criteria defined in Kauffmann et al. (2003).

The Dopita et al. (2016) calibration uses only the Hα, [N II], and [S II] emission lines, all located in a very narrow spectral interval and is, therefore, virtually insensitive to the internal extinction within an observed galaxy. This calibration is presented in the form of a simple formula, which makes it very easy to use. However, a disadvantage of this approach in

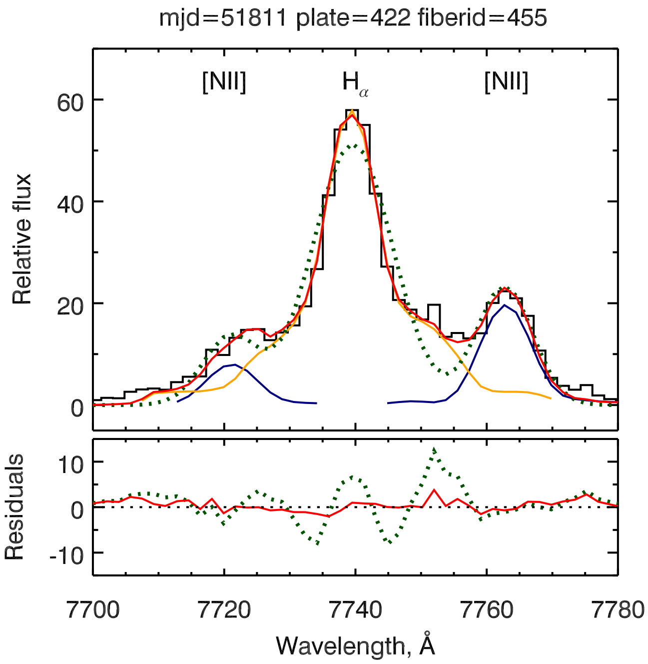

Figure 5. Example of the complex emission line profile of a Seyfert galaxy, and the results of its fitting with two different techniques. The black stepped line in the upper panel shows the observed spectrum of Hα and N II lines in relative flux units, the green dotted line is a Gaussian fit result, and the red solid line is a non-parametric fitting result. Individual Hα and N II profiles recovered by the non-parametric fitting are shown in orange and blue, respectively. The lower panel shows the fitting residuals. In the case of complex asymmetric emission line profiles, the non-parametric fitting method is clearly preferred over the Gaussian one.

application to our data set is that at redshifts $z > 0.1$ the emission lines used for the metallicity determination shift to the spectral region dominated by telluric absorption and airglow emission lines (mostly OH), which can seriously affect the quality of the emission line flux estimates. Another natural limitation of this approach originates from the SDSS spectral wavelength range ($\lambda < 9200$ Å) that corresponds to the upper redshift limit $z = 0.36$ when the forbidden sulfur line [S II] 6730 Å shifts out of the wavelength range. Further, the calibration critically depends on the [N/O] relation and is therefore sensitive to possible galaxy to galaxy [N/H] abundance variations. In the catalog, we included the metallicity estimates obtained using the Dopita et al. (2016) calibration for Gaussian emission line analysis (`rcsed_gasmet` table). We computed the uncertainties of the gas phase metallicities by propagating the statistical flux errors through the calculations according to the formula in Dopita et al. (2016).

The IZI technique (Blanc et al. 2015) takes advantage of all available emission line measurements and, hence is more robust and can in principle be used for the entire sample of SDSS galaxies. The algorithm is implemented in an IDL software package distributed by the authors along with 17 grids of photoionization models. However, this technique relies on external dust attenuation correction, which must be applied to emission line fluxes prior to fitting. It also requires (similar to the Dopita et al. 2016 approach) a pre-selection of star-forming galaxies. We estimated the internal dust attenuation using the typical value of the Balmer decrement Hα/Hβ = 2.83 (Groves et al. 2012) and corrected all emission line fluxes accordingly. In galaxies where the observed Hα/Hβ ratio fell below that value, we assumed the extinction to be zero. Finally, the fluxes were supplied to the IZI software package with the Dopita et al. (2013) model grid, and the resulting [O/H] and ionizing parameter values for Gaussian emission line fluxes were included in the gas phase metallicity table, `rcsed_gasmet`, of the catalog.

3. Photometric Properties of the Sample

3.1. Completeness at Different Redshifts

Because our catalog uses the SDSS DR7 spectroscopic galaxy sample as its master list, and the legacy SDSS spectroscopic survey was magnitude limited with the $r = 17.77$ mag limit in a 3 arcsec aperture, we sample different parts of the galaxy luminosity function with the redshift-dependent completeness. Also, there is an important fiber collision effect, which means two fibers in the SDSS multi-object spectrograph cannot be put too close to each other: because of this, there is a systematic undersampling of dense clusters and groups of galaxies. Q1

In Figure 6 (top panel) we present a two-dimensional distribution of our galaxies in the (M_z, $g - r$) color–magnitude space. We identify the regions traditionally referred to as "the red sequence" and "the blue cloud" as well as the locus of typical post-starburst (*E+A*) galaxies. The density in the plot corresponds to the object number density in our catalog at a given position in the parameter space. We also show by small crosses the tidally stripped systems, compact elliptical galaxies, from the sample of Chilingarian & Zolotukhin (2015), which reside systematically above the red sequence. One can see the bimodality of the galaxy distribution by color for intermediate-luminosity and dwarf galaxies ($M_z > -20.5$ mag), while the transition is rather smooth for more luminous systems.

Even though dwarf galaxies are more numerous in the universe than giants because of the rising low end of the galaxy luminosity function (Schechter 1976; Blanton et al. 2003), we see the apparent decrease of the histogram density at fainter magnitudes. In the bottom panel of Figure 6, we demonstrate the breakdown by redshift for the luminosity distribution of galaxies contributing to the histogram in the top panel. The ~~high luminosity-end decline~~ is due to the intrinsic shape of the luminosity function, while the low luminosity tail drops because of the SDSS completeness and target selection biased against very extended (and therefore nearby) galaxies. We clearly see how the magnitude-limit constraint of SDSS causes the drop in the number of galaxies further and further up the luminosity function as we move to higher redshifts. Figure 6 confirms that we start probing the dwarf galaxy regime ($M_z > -19.8$ mag) at $z < 0.06$; however, the selection effects have to be seriously considered for any type of statistical study.

3.2. Red Sequence in Different Bands

For practical reasons such as selection of candidate early-type members in galaxy clusters using photometric data, it is important to know the shape of the red sequence in different photometric bands. Here we provide the best-fitting second-degree polynomial approximations of the red-sequence shape for a set of galaxy colors spanning optical and NIR bands.

First, we created a sample of red sequence galaxies using the following criteria: (1) we selected all objects at redshifts $z < 0.27$; (2) we applied a color cut on NUV $- r$ colors by selecting all objects on the (M_r, NUV $- r$) plane that resided above the straight line passing through $p_0 = (-16.0, 3.5)$ mag and $p_1 = (-24.0, 5.0)$ mag, (3) we applied a color cut on $g - r$ colors by selecting all objects on the $(M_r, g - r)$ plane that resided above the straight line passing through $q_0 = (-16.0, 0.5)$ mag and $q_1 = (-24.0, 0.75)$ mag and also satisfying the criterion $(g - r) < 0.95$ mag.

Then, in order to account for the two-order-of-magnitude variations of galaxy density along the red sequence, for every combination of colors and magnitudes (e.g., $g - r$, M_r) (1) we selected measurements having statistical uncertainties <0.1 mag in both bands; (2) binned the distribution on luminosity using 0.5 mag-wide bins and computed median color values and outlier resistant standard deviations in every bin; and (3) fitted a second-degree polynomial into median values only in those bins that contained more than 15 objects. For convenience and because mean absolute *AB* magnitudes of galaxies in our sample stay mostly within the range $-25 < M < -15$ mag in all optical red (*riz*) and NIR filters, we added 20.0 mag to all absolute magnitudes prior to fitting:

$$
\begin{aligned}
(u-r) &= +2.51 - 0.065 \cdot M_{20r} - 0.005 \cdot M_{20r}^2;\ \sigma = 0.16\\
(u-i) &= +2.90 - 0.069 \cdot M_{20i} - 0.007 \cdot M_{20i}^2;\ \sigma = 0.17\\
(u-z) &= +3.15 - 0.050 \cdot M_{20z} - 0.014 \cdot M_{20z}^2;\ \sigma = 0.19\\
(g-r) &= +0.75 - 0.026 \cdot M_{20r} - 0.001 \cdot M_{20r}^2;\ \sigma = 0.045\\
(g-i) &= +1.12 - 0.038 \cdot M_{20i} - 0.003 \cdot M_{20i}^2;\ \sigma = 0.074\\
(g-z) &= +1.39 - 0.044 \cdot M_{20z} - 0.009 \cdot M_{20z}^2;\ \sigma = 0.10\\
(g-Y) &= +1.91 - 0.067 \cdot M_{20Y} - 0.018 \cdot M_{20Y}^2;\ \sigma = 0.14\\
(g-J) &= +2.01 - 0.073 \cdot M_{20J} - 0.016 \cdot M_{20J}^2;\ \sigma = 0.18\\
(g-H) &= +2.30 - 0.094 \cdot M_{20H} - 0.015 \cdot M_{20H}^2;\ \sigma = 0.19\\
(g-K) &= +2.00 - 0.108 \cdot M_{20K} - 0.018 \cdot M_{20K}^2;\ \sigma = 0.22\\
M_{20\mathrm{col}} &= M_{\mathrm{col}} + 20.0\ \mathrm{mag}.
\end{aligned}
\tag{1}
$$

Equations (1) provide the best-fitting polynomials for the red-sequence shape in 10 photometric bands. We consider the mean standard deviation value from all bins used in the fitting procedure as the "red sequence width" (σ in Equations (1)) and stress that the actual fitting residuals for median values are usually an order of magnitude smaller.

We note that in the most widely used parameter spaces, $(M_r, g - r)$, $(M_r, u - r)$, $(M_i, g - i)$, and $(M_z, g - z)$, the red sequence does not show any substantial curvature, which is indicated by negligible second-order polynomial terms. This suggests that there is no "red sequence saturation" at the bright end.

3.3. Color Transformations for Galaxies of Different Morphologies and Luminosities

Chilingarian & Zolotukhin (2012) demonstrated that the Hubble morphological classification derived by human eye (Fukugita et al. 2007) correlates very well with the total NUV − r color of a galaxy. With a computed dispersion of $0.8t$, where t is the Hubble type, it corresponds to the subjective precision of such a classification. Here we use this relation in order to derive median values of galaxy colors across the Hubble sequence for three galaxy luminosity classes defined on the basis of their r-band luminosities.

We dissect the $(M_r$, NUV $- r)$ color–magnitude plane into 18 quadrangular regions by assuming that the morphological

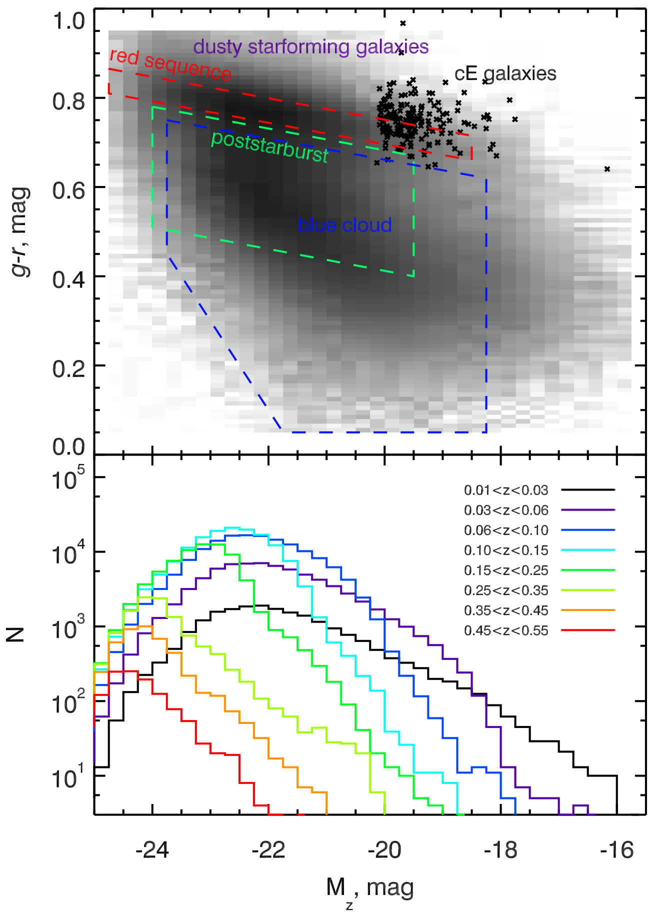

Figure 6. (Top) Optical color–magnitude diagram for extinction- and k-corrected Petrosian magnitudes of all galaxies in our sample. (Bottom) Redshift distributions of galaxies in corresponding bins of absolute magnitude.

type for giant galaxies ($M_r = -24$ mag) can be estimated by linearly varying the (NUV $- r$) color from +0.5 to +6.5 mag with a step of 1 mag corresponding to one Hubble type from *Sd* to *E*. At the same time, we assume that in the dwarf regime ($M_r = -16$ mag) the step reduces to 0.75 mag per Hubble type, which corresponds to the observed reduction of the (NUV $- r$) color range. We choose three luminosity bins, $-24.0 \leqslant M_r < -22.0$ mag, $-22.0 \leqslant M_r < -19.0$ mag, and $-19.0 \leqslant M_r < -16.0$ mag, which represent giant, intermediate luminosity, and dwarf galaxies. Then, in every region we compute the median value of the desired color and the standard deviation of the distribution.

We present our results in Table 3. They expand and update the widely used color transformations from Fukugita et al. (1995) by using a very rich data set properly corrected for systematic effects and using modern prescriptions for k-corrections. We extend their results at $z = 0$ (see Table 3 in Fukugita et al. 1995) to near-UV and NIR colors and also toward intermediate- and low-luminosity galaxies. The direct comparison of our values with those of Fukugita et al. (1995) reveals a good agreement of optical colors except for (a) S0 galaxies, which are systematically redder in our case and stay really close to the ellipticals, and (b) the $u - g$ color of ellipticals, which is some 0.25 mag bluer in our case. We assign the latter systematics to our improved k-correction prescriptions for the u-band photometry and generally higher quality of the u-band SDSS photometric data compared to the

Table 3
Median Rest-frame Colors of Galaxies of Different Morphological Types and Luminosities in *AB* Magnitudes

	$-24.0 \leqslant M_r < -22.0$ mag						$-22.0 \leqslant M_r < -19.0$ mag						$-19.0 \leqslant M_r < -16.0$ mag					
	Sdm	Sc	Sb	Sa	S0	E	Sdm	Sc	Sb	Sa	S0	E	Sdm	Sc	Sb	Sa	S0	E
FUV–*r*	1.72	2.76	3.46	4.33	5.58	6.86	1.60	2.48	3.22	4.15	5.22	6.72	1.44	2.18	2.87	3.81	4.91	6.78
stdev	0.33	0.33	0.40	0.50	0.78	0.67	0.31	0.32	0.39	0.48	0.71	0.78	0.26	0.31	0.36	0.46	0.75	0.91
NUV–*r*	1.20	2.20	2.89	3.73	4.84	5.64	1.17	2.02	2.69	3.57	4.57	5.44	1.15	1.80	2.41	3.29	4.18	4.98
stdev	0.26	0.20	0.27	0.29	0.30	0.25	0.22	0.24	0.27	0.28	0.29	0.27	0.18	0.23	0.24	0.25	0.26	0.25
u–*r*	0.99	1.48	1.80	2.14	2.44	2.56	0.95	1.34	1.68	2.05	2.32	2.44	0.88	1.19	1.44	1.76	2.02	2.14
stdev	0.15	0.19	0.21	0.21	0.23	0.19	0.19	0.20	0.20	0.21	0.21	0.17	0.26	0.20	0.19	0.22	0.24	0.21
g–*r*	0.26	0.49	0.60	0.70	0.78	0.80	0.24	0.40	0.53	0.65	0.73	0.76	0.22	0.34	0.45	0.57	0.66	0.69
stdev	0.15	0.06	0.05	0.05	0.05	0.03	0.09	0.07	0.06	0.05	0.05	0.04	0.10	0.06	0.06	0.06	0.06	0.04
g–*i*	0.42	0.75	0.92	1.06	1.15	1.17	0.33	0.58	0.81	1.00	1.10	1.12	0.26	0.45	0.64	0.85	0.98	1.02
stdev	0.27	0.11	0.09	0.07	0.07	0.05	0.16	0.12	0.11	0.08	0.08	0.06	0.16	0.11	0.10	0.11	0.10	0.07
g–*z*	0.66	0.97	1.16	1.32	1.42	1.44	0.41	0.72	1.02	1.25	1.37	1.39	0.33	0.55	0.79	1.05	1.18	1.24
stdev	0.32	0.18	0.14	0.11	0.10	0.07	0.21	0.18	0.16	0.12	0.11	0.09	0.21	0.18	0.16	0.16	0.15	0.10
g–*Y*	1.27	1.50	1.70	1.87	1.97	1.98	0.78	1.12	1.50	1.79	1.91	1.92	0.59	0.82	1.12	1.46	1.58	1.68
stdev	0.45	0.19	0.17	0.13	0.12	0.09	0.31	0.27	0.22	0.16	0.14	0.12	0.33	0.28	0.26	0.26	0.23	0.15
g–*J*	1.37	1.56	1.77	1.96	2.05	2.07	0.83	1.15	1.58	1.90	2.01	2.03	0.53	0.77	1.11	1.51	1.66	1.75
stdev	0.46	0.23	0.21	0.17	0.16	0.13	0.38	0.35	0.27	0.19	0.18	0.15	0.49	0.46	0.39	0.36	0.32	0.22
g–*H*	1.63	1.87	2.10	2.30	2.39	2.40	1.05	1.42	1.89	2.22	2.33	2.33	0.77	1.02	1.37	1.80	1.89	1.99
stdev	0.54	0.24	0.21	0.18	0.17	0.14	0.39	0.35	0.27	0.21	0.20	0.16	0.47	0.38	0.34	0.36	0.32	0.20
g–*K*	1.54	1.61	1.83	2.03	2.11	2.11	0.80	1.12	1.60	1.95	2.04	2.03	0.34	0.62	1.00	1.44	1.55	1.63
stdev	0.52	0.25	0.23	0.19	0.18	0.15	0.45	0.40	0.30	0.24	0.23	0.18	0.56	0.49	0.42	0.44	0.36	0.24

Note. For every color (left column), there are three groups corresponding to giant (first group), intermediate-luminosity (second group), and dwarf (third group) galaxies, with six values for six Hubble types. Standard deviation values for each median color are presented in the adjacent table rows.

data set used in Fukugita et al. (1995). On the other hand, we attribute redder colors of lenticular galaxies in our data to the specificities of the synthetic color estimation technique used in Fukugita et al. (1995) that underestimated colors of two of four of their lenticular galaxies by 0.1–0.15 mag (see their Table 1).

4. Spectroscopic Properties of the Sample

4.1. Stellar Kinematics of Galaxies

In comparison to the original SDSS measurements of stellar kinematics based on cross-correlation with a limited set of template spectra, our approach yields a significantly smaller template mismatch between models and observed spectra for non-active galaxies. We, therefore, achieve on average 30% lower statistical uncertainties on the radial velocity and velocity dispersion measurements. Moreover, there is a known degeneracy between stellar metallicity and velocity dispersion estimates when using pixel-space fitting techniques (Chilingarian et al. 2007b), because an underestimated metallicity (i.e., using a metal-poor template for a metal-rich galaxy) can be compensated by a lower velocity dispersion that would smear that template spectrum by a lesser degree. Therefore, by using a grid of stellar population models ranging from low ([Fe/H] $= -2.0$ dex) to high ([Fe/H] $= +0.7$ dex) metallicities and covering the entire range of ages, we reduce the systematic errors of the velocity dispersion measurements, especially in the most metal-rich regime including massive elliptical and lenticular galaxies. On the other hand, we accurately take into account the spectral line spread function of the SDSS spectrograph that allows us to measure velocity dispersions down to 50 km s^{-1}, thus going far into the dwarf galaxy regime (Chilingarian 2009).

As already pointed out by Fabricant et al. (2013), stellar velocity dispersion measurements in the SDSS DR7 catalog are systematically underestimated for luminous elliptical galaxies compared to the values obtained by the full spectrum fitting, which is likely caused by the template mismatch and degeneracy with metallicity mentioned above. Here we observe a very similar trend: our SSP velocity dispersion measurements for massive ellipticals ($\sigma \gtrsim 250$ km s^{-1}) are up to 30 km s^{-1} higher than those reported in the SDSS DR7 catalog, and this difference goes down to 7–10 km s^{-1} for low luminosity galaxies ($\sigma \sim 100$ km s^{-1}). In Figure 7 (top panel), we present the comparison made for our entire sample for 361,421 galaxies with velocity dispersion uncertainties better than 7% of the value (i.e., $\Delta\sigma = 7$ km s^{-1} for $\sigma = 100$ km s^{-1}). The velocity dispersions estimated from the fitting of exponentially declining SFH models computed with PEGASE.HR are a little bit closer to the values in SDSS DR7; however, the general trend looks similar (Figure 7, bottom panel).

In Figure 8 we present the relation between the galaxy luminosities and velocity dispersions—the Faber–Jackson (Faber & Jackson 1976) relation—constructed for the 52,506 elliptical galaxies that were morphologically selected by the Galaxy Zoo (Lintott et al. 2011) citizen science project and had statistical uncertainties of their velocity dispersion measurements better than 10% of the value. We have corrected velocity dispersion measurements to their global values according to Cappellari et al. (2006) using half-light radii from Simard et al. (2011) included in our catalog. We used the criterion formulated in Saulder et al. (2013): in order to be included in our early-type galaxy sample, an object has to be classified by at least 10 Galaxy Zoo users, at least 70% of whom classify it as an elliptical galaxy. Six panels present measurements in six different redshift intervals, shown as dots, while the contours display the cumulative distribution at all redshifts. The lowest redshift panel contains the measurements for a sample of galaxies in the Abell 496 cluster ($z = 0.033$) obtained from the analysis of intermediate resolution ($R = 6300$) spectra collected with the FLAMES–Giraffe spectrograph at the 8 m Very

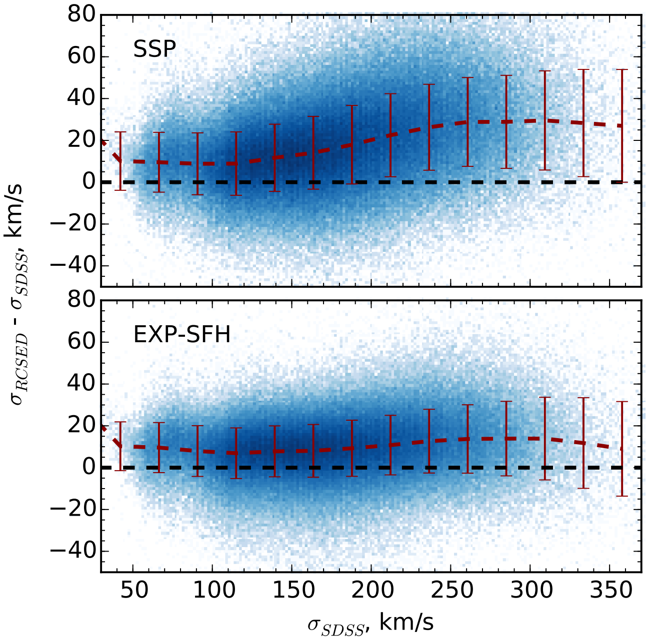

Figure 7. Comparison of RCSED stellar velocity dispersion measurements with those published by the SDSS DR7. Top and bottom panels correspond to the two sets of stellar population models, SSP, and exponentially declining SFHs, respectively.

Large Telescope of the European Southern Observatory (Chilingarian et al. 2008). This data set comprises mostly dwarf early-type galaxies, and it clearly forms an extension of the low-luminosity part of the relation formed by the SDSS galaxies, which demonstrates that our velocity dispersion measurements at the low end do not suffer from the systematic errors connected to the spectral line spread function uncertainties. The red dashed line represents the Faber–Jackson relation for giant elliptical galaxies $L_g \propto \sigma^{4.00}$ at $z = 0$ presented in Bernardi et al. (2003). We see that the slope changes to $L_g \propto \sigma^{2.00}$ at fainter luminosities $M_g > -19.5$ mag similar to what was demonstrated for a sample of dwarf galaxies in the Coma galaxy cluster by Matković & Guzmán (2005).

Because of the correlation of the galaxy luminosity with the stellar velocity dispersion and magnitude-limited input galaxy sample, higher redshift galaxies contribute only to the bins at high stellar velocity dispersions. Our catalog probes dwarf galaxies ($\sigma < 100$ km s^{-1}) at low redshifts ($0.007 < z < 0.06$) that includes hundreds of massive galaxy clusters and groups.

RCSED velocity dispersion measurements were used prior to publication by Saulder et al. (2013) to calibrate the fundamental plane (FP; Djorgovski & Davis 1987). We refer to that work for an intensive discussion regarding the FP of elliptical galaxies observed by the SDSS.

4.2. Stellar Populations from Absorption Line Analysis

In our catalog we include stellar population parameters obtained by the fitting of galaxy spectra using two stellar population model grids computed with the PEGASE.HR evolutionary synthesis code: (i) SSP models based on the intermediate resolution MILES stellar library characterized by ages (t) and metallicities ([Fe/H]) and (ii) models with exponentially declining SFHs based on the high-resolution ELODIE-3.1 stellar library characterized by exponential timescales (τ) and metallicities ([Fe/H]). In Figure 9, we present distributions of galaxies in the two-parameter spaces.

One can clearly see a spotty structure in the SSP best-fitting results and the lack of such a structure for exponentially decaying models. We also performed similar tests for original MILES stellar population models by Vazdekis et al. (2010) and models by Bruzual & Charlot (2003) for a subsample of SDSS DR7 spectra. We will provide a complete description and detailed discussion in a forthcoming paper (~~Katkov et al. 2016,~~ in preparation). Here we present a brief summary and conclusions of our study. Q2

The observed spotty structure represents artifacts caused by the improper implementation of the interpolation algorithm in the stellar population code, most likely in the stellar library interpolation step propagating into stellar population models, and not by the NBURSTS population-fitting procedure. The NBURSTS code uses a nonlinear minimization technique that requires the second partial derivatives on all parameters to be continuous. Discontinuities will cause the solution to be either attracted to some region of the parameter space or pushed away from it.

Our conclusion is supported by the following observations: (i) the morphology of the spotty structure remains very similar when using two different sets of SSP models computed with the same PEGASE.HR code but with different stellar libraries, MILES and ELODIE; (ii) switching to original MILES models (Vazdekis et al. 2010) where the interpolation procedure is much simpler than in PEGASE.HR (linear interpolation between the five nearest neighbors) changes the structure completely and strengthens the artifacts, (iii) using exponentially decaying star formation models that are constructed from numerous weighted SSPs removes most of the pattern at $\tau \gtrsim 1.0$ Gyr but the structure still holds at $\tau < 1.0$ Gyr where the number of co-added SSPs is small, and (iv) smoothing a grid of PEGASE.HR MILES-based SSP models using basic splines (b-splines) on the age removes most of the pattern.

We also notice that extending the working wavelength range to shorter wavelengths (<4500 Å) and increasing the multiplicative polynomial degree strengthens the pattern while leaving spot positions in the pattern virtually the same. Therefore, we chose a very low-order fifth-degree polynomial continuum and restricted the wavelength range to $\lambda > 4500$ Å for the SSP fitting that produced the stellar population parameters presented in our catalog.

In the top panel of Figure 10, we present a comparison of SSP ages and exponential timescales τ. Despite the artifact structure in ages that extends into horizontal stripes on this plot, there is a one-to-one correspondence between t and τ in a wide range of ages. Short timescales τ correspond to old stellar populations while $\tau = 20$ Gyr is equivalent to $t \approx 1.8$ Gyr. The relation "saturates" for younger stellar populations because they cannot be represented by exponentially declining SFHs starting at high redshifts: either a later start or multiple star formation episodes are needed to describe them. Chilingarian & Zolotukhin (2012) demonstrated that exponentially declining SFHs much better represent observed broadband optical and UV colors than SSP models. In our current sample, about 16% of galaxies (~131,500) have stellar populations too young to be described by exponentially declining SFHs.

The bottom panel of Figure 10 displays the comparison of stellar metallicities for the two sets of models. The agreement is very good, with a slight systematic difference

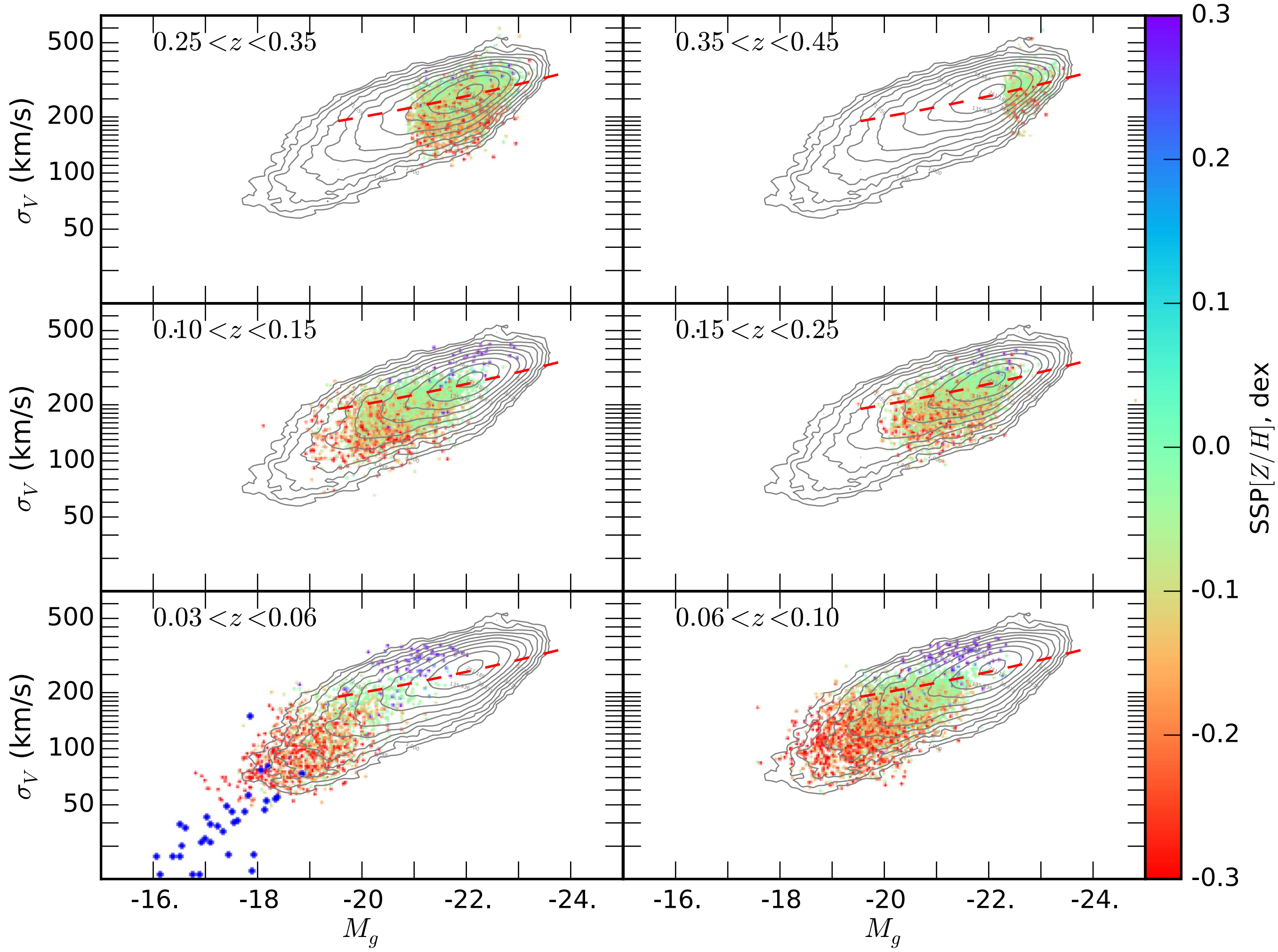

Figure 8. Faber–Jackson relation for 52,506 morphologically classified elliptical galaxies in our sample (Galaxy Zoo classification). In order to remove outliers, a 10% cut was applied on the relative errors on the g magnitude and on the velocity dispersion, and a good adjustment $\chi^2 < 0.8$ was required. The contours correspond to the whole sample (smoothed with a 3×3 pixel window). Each panel displays a redshift range corresponding to Figure 6. The color coding corresponds to the SSP metallicity $[Z/H]$ displayed in Figure 10. The dashed red line corresponds to the maximum likelihood estimate of the slope $L_g \propto \sigma^{4.00}$ at $z = 0$ computed by Bernardi et al. (2003). The blue points in the low redshift subsample (in the bottom-left panel) correspond to the dwarf galaxy sample of Chilingarian et al. (2008).

between $-0.6 < [\mathrm{Fe/H}] < -0.2$ dex, which we attribute to the degeneracy between the metallicity and velocity dispersion measurements for intermediate S/Ns.

We clearly see a substantial degeneracy between the metallicity and velocity dispersion estimates which was pointed out in Chilingarian et al. (2007b). In order to perform a clear test, free of any effects connected to the use of different star-formation histories, we fitted a subset of ~420,000 spectra using PEGASE.HR SSP models in the wavelength range 3910–6790 Å and compared the metallicity and velocity dispersion measurements to those obtained from the fitting of MILES–PEGASE models against the same spectra. In Figure 11 we present the relation between the differences in velocity dispersions and SSP metallicities obtained using the two sets of models at different S/Ns. We can clearly see the degeneracy manifested by the elongated shape of the cloud that decreases with increasing S/N, up to the S/N of 30. Above 30 the improvement becomes insignificant. This result suggests that published velocity dispersion values obtained with the full spectral fitting of intermediate-resolution spectra $R = 1500$–2500 are subject to serious systematic errors reaching 15% of the measured value.

4.3. Emission Line Properties

4.3.1. Comparison of Line Fluxes with the MPA–JHU and OSSY Catalogs and Between the Two Techniques

We compare a subset of our catalog containing measurements of emission line fluxes obtained from the parametric Gaussian fitting to the results from the MPA–JHU catalog distributed by the SDSS project (Brinchmann et al. 2004; Tremonti et al. 2004) and with the OSSY catalog (Oh et al. 2011). We used OSSY emission line measurements prior to the internal extinction correction. Given that the fluxes were computed using very similar methodologies, with the main difference corresponding to the subtraction of the underlying stellar population and the Galactic extinction correction techniques used, we expect a very good agreement with well-detected emission lines. We directly compare fluxes of the [O II] (3727 Å), [O III] (5007 Å), Hα, and [N II] (6584 Å) emission lines for a sample of galaxies where they were detected at a level exceeding 10σ (i.e., Flux/σ (Flux) > 10). The results are presented in Figure 12. We obtain an excellent agreement with a systematic difference of less than 1% and standard deviation of residuals of about 2%

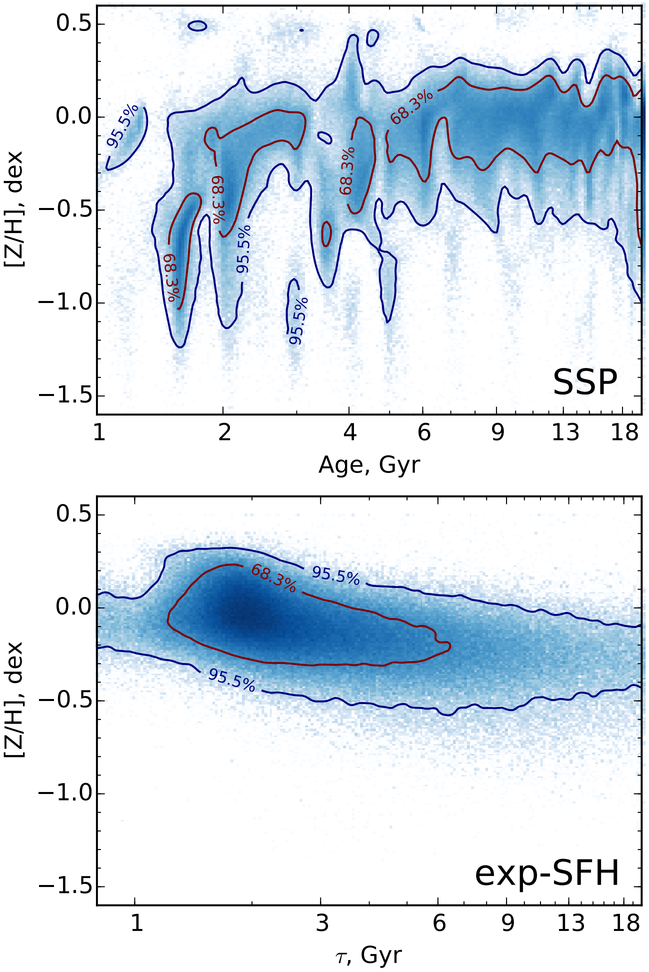

Figure 9. Distributions of galaxies in the age–metallicity space from the fitting of SSP (top panel) and exponentially decaying SFH (bottom panel) models.

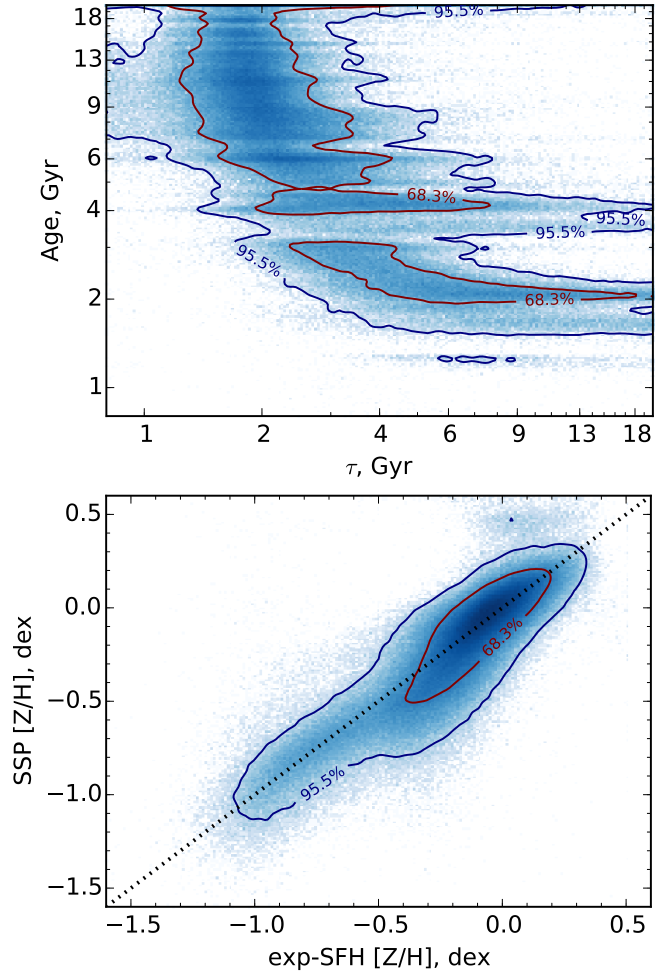

Figure 10. Comparison of SSP ages to timescales τ for exponentially decaying models (top) and metallicity measurements (bottom).

for the bright end of the Hα flux distribution. At the faint end (10σ detection), the systematic difference stays within 2% while the standard deviation grows to 3%. Hence, we conclude that our emission line fitting code works as expected and does not introduce any substantial systematic errors to the flux measurements.

Compared to Hα, the Hβ line is much more sensitive to the age of the stellar population being subtracted. In Appendix A we discuss the systematic errors of the Hβ measurements as a function of the age mismatch. In case of faint emission lines, the systematics dominates the measurements if the age was determined incorrectly, and makes them useless for emission line diagnostics.

The principal difference of our results from those published earlier is the non-parametric approach to the emission line fitting. For galaxies that exhibit some signs of nuclear activity, the Balmer lines fluxes derived non-parametrically significantly exceed the values obtained with the Gaussian fitting. In Figure 13 we present the Hα flux ratio between the two approaches. The inset contains the same Seyfert galaxy, which we presented earlier in Figure 5, and the arrow indicates its position in the diagram that suggests that its non-parametric Hα flux estimate is about 20% higher than that obtained with the Gaussian profile fitting.

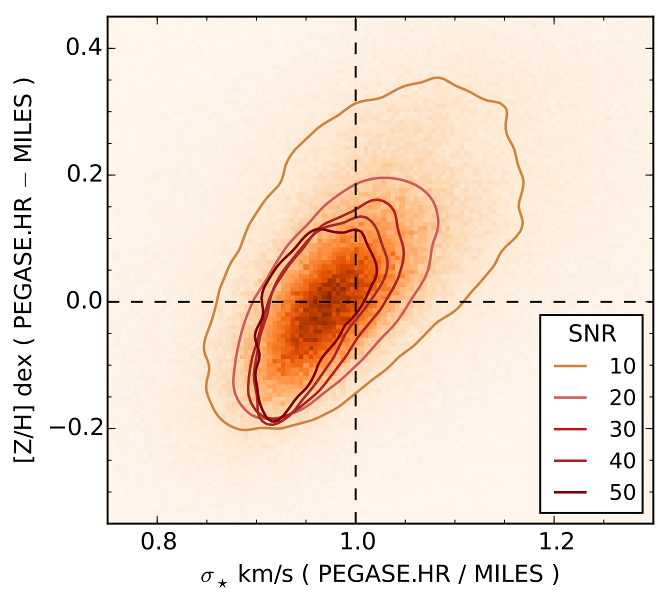

Figure 11. Degeneracy between metallicity and velocity dispersion estimates shown as the ratio between velocity dispersions vs. SSP metallicities obtained from the fitting of some 420,000 SDSS spectra using PEGASE.HR and MILES–PEGASE SSP models. The contours show the 1σ values which correspond to the areas containing 68% of the galaxies with the spectra having S/Ns within 20% of the displayed value. The number of galaxies for each contour ranges from $\sim$1800 (S/N = 50) to $\sim$111,000 (S/N = 10).

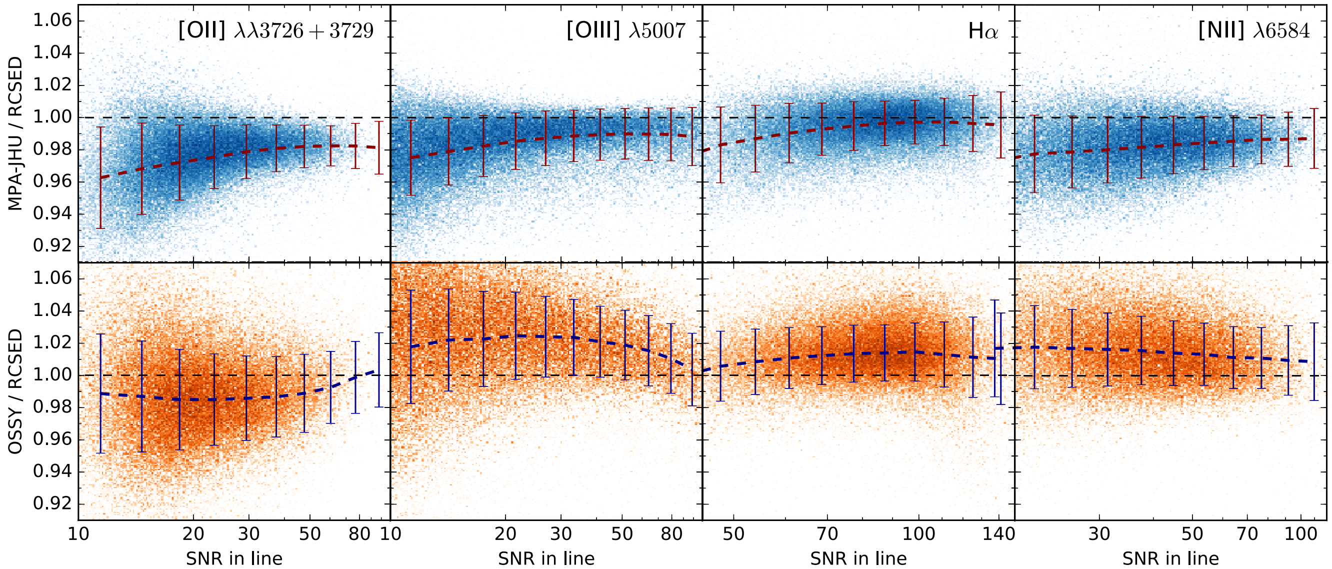

Figure 12. Comparison of RCSED Gaussian emission line fluxes for four emission lines with the MPA–JHU (top row of plots) and OSSY (bottom row of plots) catalogs. The median and standard deviation of the distribution are shown by the brown symbols with error bars.

4.3.2. BPT Diagrams and Gas Phase Metallicities

In Figure 14 we present three flavors of the BPT diagram, using different combinations of emission lines computed with the non-parametric fitting. The points are color-coded according to the Hα emission line EW. Cid Fernandes et al. (2010) proposed using the Hα EW to discriminate between Seyfert and LINER activity (instead of the traditionally used [O III]/Hβ ratio), because Hβ is often too weak to be detected and measured. We clearly see the bimodal distribution of non-star-forming galaxies in the two bottom panels, which correspond to Seyfert galaxies (cloud to the top) and LINER/shockwave/post-AGB ionization (cloud to the bottom). The top panel displays the original BPT relation. The region between the red solid and the blue dashed lines defines the "transitional" galaxies (Kewley et al. 2006), which we included in the calculation of metallicities in addition to the star-forming galaxies located to the bottom-left part of the blue dashed line.

As we described above, RCSED includes gas phase metallicity measurements calculated with the Bayesian method implemented in the IZI software package with the Dopita et al. (2013) model grid, which uses all available emission lines in a spectrum, and a recent technique by Dopita et al. (2016) that relies on the [N/O] calibration and uses only five emission lines around Hα.

Kewley & Ellison (2008) demonstrated that different emission line calibrations yield largely inconsistent gas phase metallicity estimates when applied to the same input data set, with the differences reaching 0.7 dex (5 times). There is currently no consensus in the astronomical community about which calibrations produce more reliable metallicity estimates with arguments for both direct (Andrews & Martini 2013) and indirect (López-Sánchez et al. 2012) methods. Gas and stellar metallicities also seem to strongly disagree (Yates et al. 2012). We notice, however, that all emission line calibrations result in the gas phase [O/H] mass–metallicity relations spanning a range of metallicities much lower than stellar metallicities for a given galaxy stellar mass range. All gas metallicity relations saturate at high metallicities and the saturation occurs at

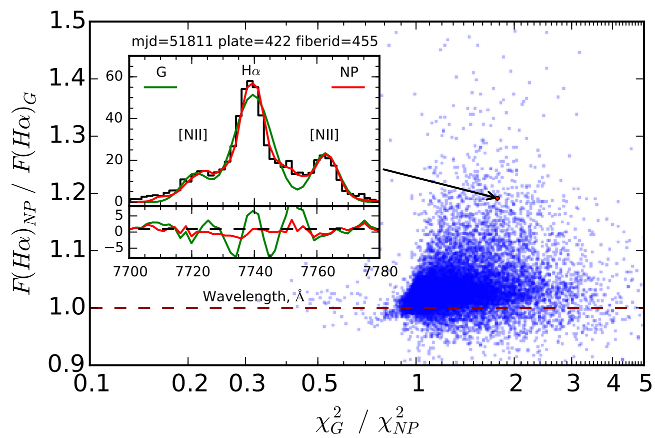

Figure 13. Comparison of the Hα fluxes obtained for the parametric (Gaussian) and non-parametric emission line profile fitting as a function of the χ^2 ratio. An example profile decomposition is shown in the inset for an object with highly discrepant flux estimates.

different values (see, e.g., Figure 10 in Andrews & Martini 2013). The highest range of metallicities is covered by the calibration used by Tremonti et al. (2004) and provided in the MPA–JHU catalog.

In Figure 15 we present the comparison of the Dopita et al. (2016) calibration with the MPA–JHU metallicities (blue shaded area) for 231,107 galaxies with the S/Ns of the Hα, [N II], [O II], and [O III] lines exceeding 10. The agreement is very good at $12 + [O/H] < 9$ dex, with the standard deviation of the difference of 0.08 dex. At higher abundances, Dopita et al. (2016) metallicities become slightly higher than those from the MPA–JHU data set.

We ran the IZI metallicity determination code for a small subsample of 20,000 randomly selected star-forming galaxies with high S/N emission lines ($S/N > 10$) using all available grids of models and compared the derived metallicities with those obtained with the Dopita et al. (2016) calibration for the same galaxy sample. The only model grid that demonstrated satisfactory agreement was that from Dopita et al. (2013). As

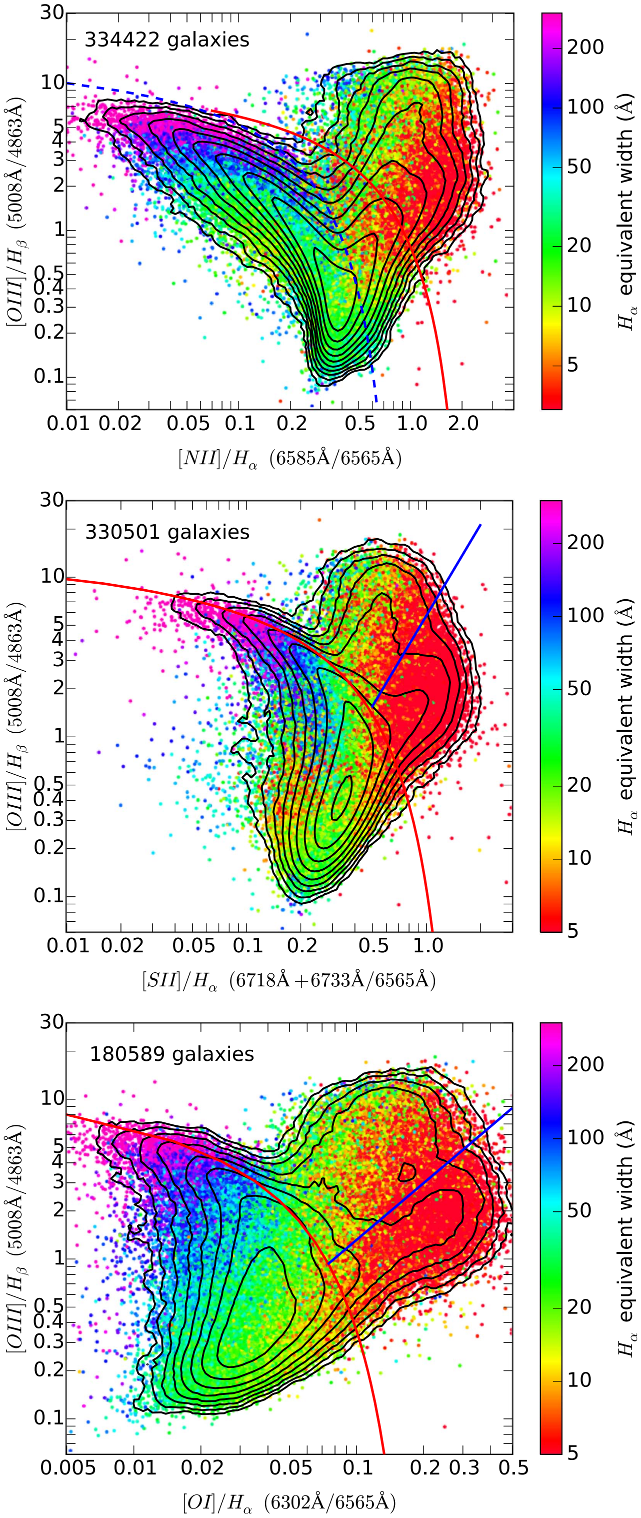

Figure 14. Three flavors of a BPT diagram with the color-coded H_α equivalent width. In each panel we display only those galaxies where all emission lines used in the corresponding plot have $S/N > 3$. The contours correspond to the galaxy density smoothed with a moving average based on a 4×4 pixel window. The number of galaxies kept in the sample is indicated inside each panel. The full and dashed lines correspond to star-forming and transitional galaxies in Kewley et al. (2006).

expected, it also provides satisfactory agreement with the MPA–JHU catalog (see Figure 15, orange shaded areas) with the standard deviation of the difference of 0.10 dex.

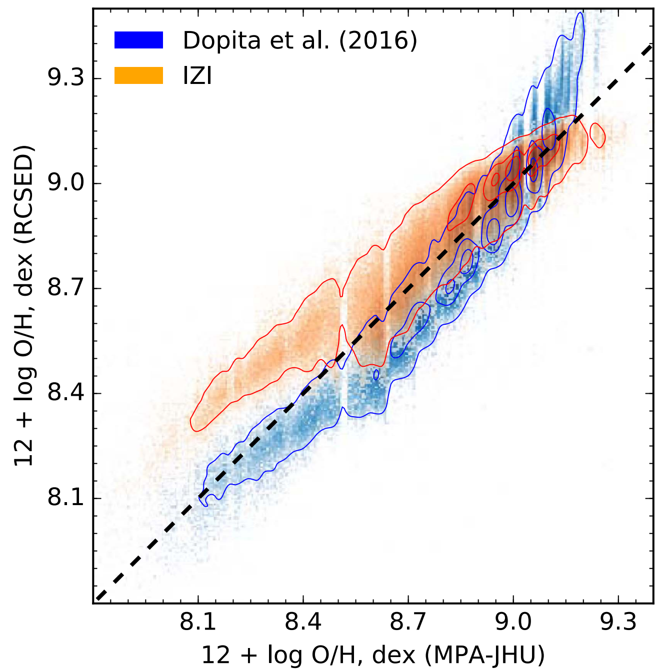

Figure 15. Comparison of gas phase metallicities published in the MPA–JHU catalog (horizontal axis) to our measurements (vertical axis). The results of the IZI Bayesian technique are shown in brown and the measurements obtained with the Dopita et al. (2016) calibration are shown in blue.

In Figure 16 we show the luminosity–metallicity relation (left panel) and the comparison of gas phase and SSP stellar metallicities (right panel) for the IZI-based determination using the Dopita et al. (2013) models (orange contours) and the Dopita et al. (2016) calibration (blue points). The mass–metallicity relation is well defined and we clearly see that the Dopita et al. (2013) model grid used in IZI yields a flatter shape than the more recent calibration (Dopita et al. 2016).

The comparison of gas phase and stellar metallicities reveals a substantial offset ranging from about 0.3 dex at solar stellar metallicities to 0.8 dex at the low end ($[\mathrm{Fe/H}]_{\mathrm{star}} = -1.1$ dex). Keeping in mind that stellar and gas phase metallicities might have different zero points and should not be directly compared to each other, the observed pattern is exactly what is expected due to the self-enrichment of stellar populations happening in galaxies with extended star-formation histories. The stars during their evolution form heavy elements which then get ejected into the ISM and recycled in subsequent generations of stars, hence increasing their metal abundances (see e.g., Matteucci 1994). Therefore, younger generations of stars become more metal-rich. SSP models probe mean stellar metallicities over the entire lifetime of a galaxy weighted with the stellar M/L ratios and the star formation rate while the gas phase metallicity reflects the current chemical abundance pattern in the ISM enriched with metals. Therefore, we expect to see the offset in metallicities. On the other hand, for the constant metal production rate per solar mass, the difference at low metallicities will be higher because the metallicity scale is logarithmic; therefore, stellar metallicities should span a larger range of value compared to gas phase metallicities and the mass–metallicity relation slopes for gas will be shallower than that for stars.

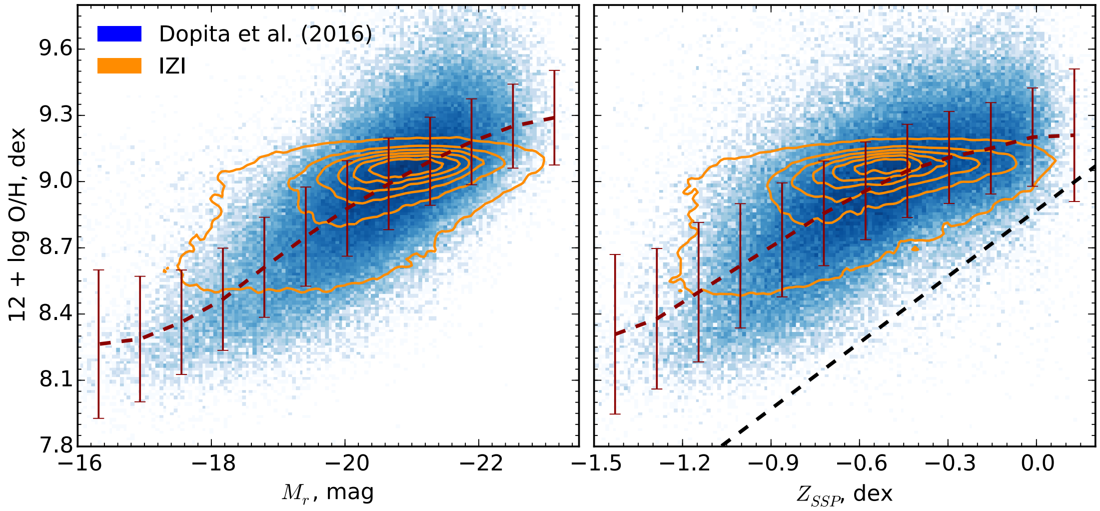

Figure 16. Relation between gas phase metallicity and galaxy luminosity (left) and an SSP stellar metallicity (right). Blue dots and orange density contours show the Dopita et al. (2016) and IZI metallicities, respectively. The median and standard deviation of the Dopita et al. (2016) measurements are shown by the brown symbols with the error bars.

5. Catalog Access: Website and Virtual Observatory Access Interfaces

Efficient, convenient, and intuitive data access mechanisms and interfaces are essential for a complex project like RCSED. Therefore, we decided to build access interfaces for both interactive and batch access to the data.

RCSED includes several different data types (e.g., spectra and tabular data), and our access infrastructure (see Figure 17) is organized to simplify their use through different interfaces. The most natural way to access the catalog is by using the web application at http://rcsed.sai.msu.ru/. It provides a single-field GOOGLE-style search interface where one can query the catalog by an object identifier, coordinates, or object properties, e.g., *select all galaxies with redshifts* $z < 0.1$ *having red colors* $g - r > 1.5$. Every object in the sample has its own web page with the summary of all its properties, SED, spectral data available in the catalog, and image cutouts displaying the object at different wavelengths provided by the *GALEX*, SDSS, and UKIDSS surveys. An example of a spectrum summary plot presented in such web pages for every object is given in Figure 4.

We developed an Application Programming Interface (API) for UKIDSS data, which allow us to extract image cutouts around an arbitrary position with a given box size in every filter. From cutout images in the *JHK* bands, we generate a color composite image and display it in the object web page. The API implemented in PYTHON is available for download from the project website. Another service we present is an interactive spectrum plotter implemented in JavaScript, our alternative to the SDSS spectrum plotter. It contains a number of value-added features, such as the display of best-fitting templates and identification of emission lines.

In addition to the custom web application, our data distribution infrastructure has the open source GAVO DaCHS[14] data center suite in its core (see Figure 17), which provides a set of VO data access mechanisms.

The data for SDSS spectra and their best-fitting SSP models are provided as FITS files that can be fetched by direct unique URLs. One can find a URL for every particular object spectrum file either in the object's web page or by querying the provided IVOA Simple Spectral Access Protocol (SSAP) web service using object coordinates. The SSAP web service answers

[14] http://soft.g-vo.org/dachs

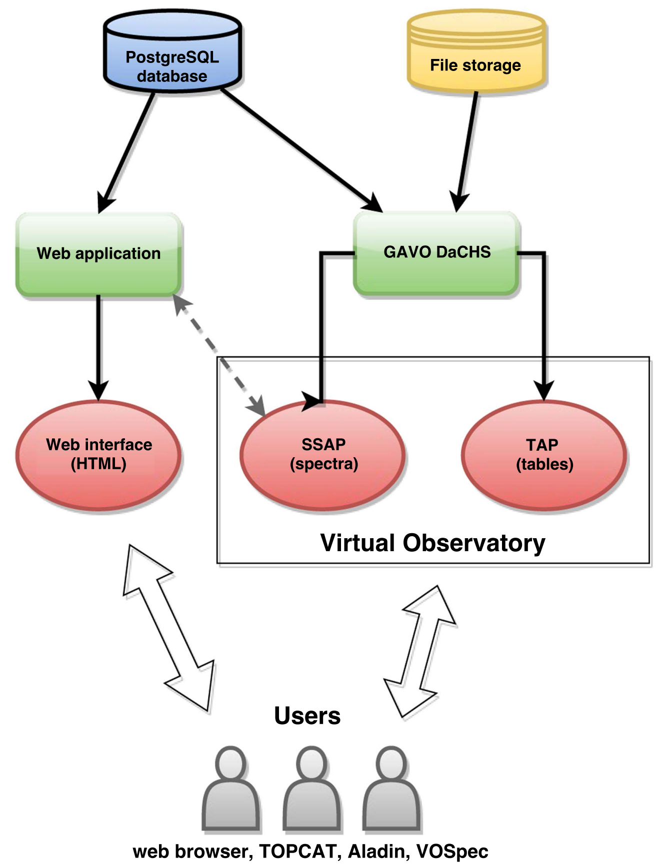

Figure 17. Block diagram of the catalog data access infrastructure. Data are stored in the relational database (catalog tables and spectra metadata) and on the disk (FITS files with spectra and continuum models). They are accessed by applications (a custom web application and the GAVO DaCHS suite) which in turn expose several public access interfaces suitable for convenient queries and data retrieval by a multitude of user client programs, both VO compatible and generic.

essentially with a list of spectra URLs and it is convenient to access programmatically or by using VO-compatible client applications such as TOPCAT[15] (Taylor 2005), SPLAT-VO,[16] Q3 or VO-Spec,[17] which can directly load spectral data for further analysis by analyzing the SSAP web service query result.

For the ultimate flexibility of querying tabular catalog data, we provide a Table Access Protocol (TAP) web service. IVOA TAP is an access interface, which allows a user to query the entire relational database schema (see Figure 18) using a powerful SQL-like language. It can be considered as an open source equivalent of the SDSS CasJobs service. Again, the TAP web service can be used for script-based access as well as by using desktop VO applications. In particular, TOPCAT has a very useful TAP query dialogue with built-in help, query examples, syntax highlighting, and given database schema assistance tools. We encourage our users to access the RCSED TAP web service through TOPCAT. We also note that our TAP service has a table upload capability, so that the user can upload his/her own tables and use it in subsequent SQL queries, i.e., in JOIN clauses, which is convenient for cross-identification of user-provided object samples with the RCSED objects without the need to download our full catalog.

Below we give several query examples that are helpful to start using the RCSED database. More query examples and science case tutorials are provided on the project website http://rcsed.sai.msu.ru. Our TAP web service can be used for joining tables from the database schema `specphot` presented in Figure 18, so that it is easy to retrieve a single table with the GalaxyZoo morphology, photometric bulge+disk decomposition, and RCSED basic parameters combined for any galaxy of interest. An example of such a query to select all those data for a particular object would be

```
SELECT
 r.*, g.*, s2.*
FROM
 specphot.rcsed AS r
 JOIN specphot.galaxyzoo AS g
  ON r.objid = g.objid
 JOIN specphot.simard_table2 AS s2
  ON r.objid = s2.objid
WHERE
 r.objid = 587731891649052703
```

Note that the `specphot` prefix for table names corresponds to the name of the database schema where RCSED tables are stored. A query to retrieve all data from the RCSED on galaxies, classified as ellipticals in GalaxyZoo, is

```
SELECT
 r.*
FROM
 specphot.rcsed AS r
 JOIN specphot.galaxyzoo AS g
  ON r.objid = g.objid
WHERE
 g.elliptical = 1
```

A query to select the data for a BPT (Baldwin et al. 1981) diagram for 10,000 galaxies with $S/N > 10$ in the corresponding line fluxes obtained with the Gaussian fitting looks like this:

```
SELECT
 TOP 10000
 f6550_nii_flx / f6565_h_alpha_flx AS BPT_x,
 f5008_oiii_flx / f4863_h_beta_flx AS BPT_y
FROM
 specphot.rcsed_lines_gauss
WHERE
 f6565_h_alpha_flx / f6565_h_alpha_flx_err >10
 AND f5008_oiii_flx / f5008_oiii_flx_err >10
 AND f4863_h_beta_flx / f4863_h_beta_flx_err >10
 AND f6550_nii_flx / f6550_nii_flx_err >10
```

Finally, all the catalog tables (see Figure 18) are available for download as FITS tables from the project's website for offline use.

6. Summary

We presented a reference catalog of homogeneous multi-wavelength spectrophotometric information for some 800,000 low- to intermediate-redshift galaxies ($0.007 < z < 0.6$) from the SDSS DR7 spectroscopic galaxy sample with value-added data. For every galaxy we provide:

1. A k-corrected and Galactic extinction-corrected far-UV to NIR broadband SED for integrated fluxes compiled from the SDSS (optical), *GALEX* (UV), and UKIDSS (NIR) surveys.
2. A k-corrected and Galactic extinction-corrected far-UV to NIR broadband SED for fluxes in circular 3 arcsec apertures that correspond to SDSS spectral apertures.
3. Results of the full spectrum fitting of an SDSS spectrum using the NBURSTS technique that includes (a) an original SDSS spectrum; (b) the best-fitting simple stellar population template in the wavelength range $3700 < \lambda < 6800$ Å and the best-fitting stellar population model with an exponentially declining star formation history in the wavelength range $3900 < \lambda < 6800$ Å; and (c) estimates of stellar radial velocities, velocity dispersions, age, an exponential characteristic timescale for the star- formation history, and metallicities for two sets of stellar population models.
4. Results of the emission line analysis using parametric (Gaussian) and non-parametric line profiles that include (a) emission line fluxes corrected for the Galactic extinction; (b) estimates of the reddening inside a galaxy for star-formation-dominated systems derived from the observed Balmer decrement; (c) radial velocity offsets with respect to stars; and (d) intrinsic emission line widths for the parametric fitting.
5. Cross-match of a galaxy with third-party catalogs providing its structural parameters from two-dimensional light profile fitting (Simard et al. 2011) and galaxy morphology from the Galaxy Zoo project (Lintott et al. 2008).

The catalog is fully integrated into the international Virtual Observatory infrastructure and available via a web application and as a Virtual Observatory resource providing IVOA TAP and IVOA SSAP interfaces in order to programmatically access tabular data and spectra, respectively.

[15] http://www.star.bris.ac.uk/~mbt/topcat/
[16] http://www.g-vo.org/pmwiki/About/SPLAT
[17] ~~http://www.sciops.esa.int/index.php?project=SAT&page=vospec~~

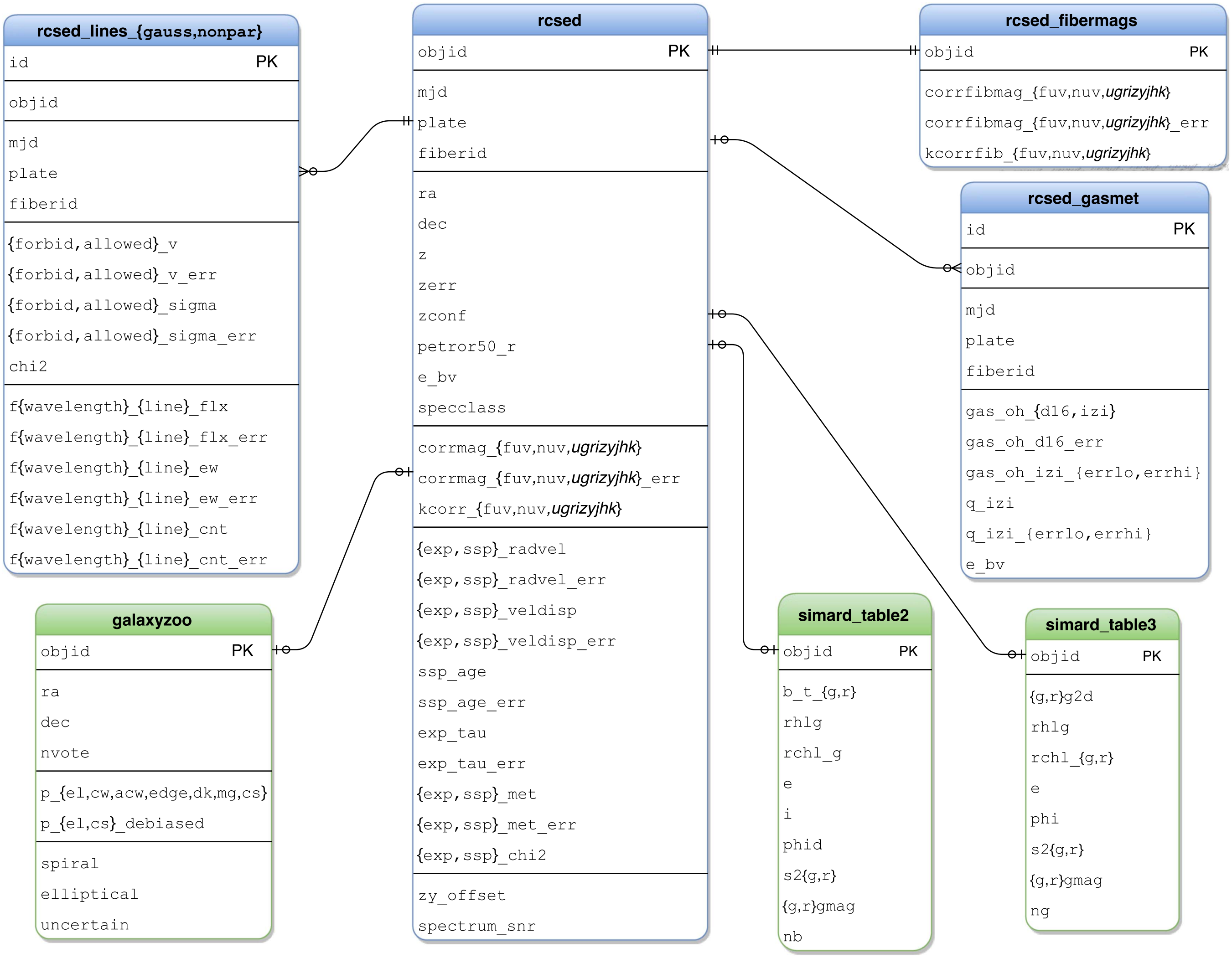

Figure 18. Entity–relationship diagram for the tables in the catalog database. Blue denotes original tables computed in RCSED, and green is for external data sets added to the database for convenience. The main table is `rcsed`, which has a one-to-one relation to the `rcsed_fibermags` table through the primary key column `objid`, a one-to-many (optional) relation to the `rcsed_gasmet` table with gas phase metallicity measurements, one-to-many (optional) relations to the `rcsed_lines_gauss` and `rcsed_lines_nonpar` tables with parametric (Gauss) and non-parametric emission line measurements. The `galaxyzoo`, `simard_table2`, and `simard_table3` data sets are all linked to the main table by the `objid` column and provide morphological classification and structural properties of galaxies from our sample using the data form Lintott et al. (2011) and Simard et al. (2011), respectively. All these tables are stored in the `specphot` database schema, so the properly qualified table name is, for example, `specphot.rcsed`. We also note that all column names in the database are in lowercase for homogeneity. The same schema and relationships apply to the distribution of RCSED in the form of FITS tables available for download from the project's website.

In addition to that, we presented best-fitting polynomial approximations for the red-sequence shape in color–magnitude diagrams that include different colors and mean colors for galaxies of six morphological types, from elliptical to late-type spirals and irregulars, and three luminosity classes (giants, intermediate luminosity, dwarfs).

Our catalog has already been used in several research projects, which can be categorized into two groups: (i) statistical studies of galaxy properties and (ii) search and discovery of rare galaxies.

The first interesting result obtained with RCSED was the discovery of a universal three-dimensional relation of NUV and optical galaxy colors and luminosities (Chilingarian & Zolotukhin 2012). It also demonstrated that the integrated NUV $-r$ color is a good proxy for morphological type. The spectrum-fitting results for elliptical galaxies were later used in the recalibration of the FP in SDSS (Saulder et al. 2013), which allowed us to compute redshift-independent distances to early-type galaxies. Finally, we performed a calibration of near-infrared stellar M/L ratios using optical colors and computed stellar masses for a new catalog of groups and clusters combining SDSS and 2MASS redshift survey data (Saulder et al. 2016). Our non-parametric emission line fitting results will be used to perform massive determinations of virial black hole masses in AGNs (~~Katkov et al. 2016, in preparation~~). Other potential applications of statistical studies based on RCSED include but are not limited to environmental dependence of galaxy-scaling relations and stellar population properties, connecting AGNs to stellar populations in galaxy centers, and comparing different star formation rate indicators (e.g., emission line fluxes, and UV and MIR photometry).

Thanks to the unique combination of photometric and spectral data as well as the physical properties of the galaxies derived from them, RCSED becomes an efficient search tool for rare or unique galaxies. Our data set was used to discover and characterize massive compact galaxies at intermediate redshifts

$0.2 < z < 0.8$ (Damjanov et al. 2013), which were thought to exist only in the early universe ($z > 1.5$), and measure their volume density (Damjanov et al. 2014). Then, using their FP positions, intermediate-redshift compact galaxies were shown to be an extension of normal ellipticals to the compact regime (Zahid et al. 2015). Finally, it was demonstrated that some massive compact early-type galaxies actually stopped forming stars very recently (Zahid et al. 2016). We also used the universal UV–optical-color–color–magnitude relation to define complex selection criteria and discover 195 previously considered extremely rare compact elliptical galaxies (Chilingarian & Zolotukhin 2015). One can identify other obvious extragalactic rarities easily searchable with RCSED: post-starburst galaxies, candidate double-peaked AGNs, dwarf AGN hosts, and "normal" galaxies with peculiarities detectable in multiwavelength data such as ellipticals with NUV excess.

In the future, we anticipate releasing intermediate- and high-redshift extensions of our catalog that will include analysis of publicly available spectra from the Smithsonian Astrophysical Observatory Hectospec archive[18] collected with the Hectospec multifiber spectrograph (Fabricant et al. 2005) the 6.5 m MMT and the DEEP2 galaxy redshift survey (Newman et al. 2013) made with the DEIMOS spectrograph at the 10 m Keck telescope. We also plan to expand the wavelength coverage by adding the all-sky infrared data from the *Wide-field Infrared Survey Explorer* satellite (Wright et al. 2010). A major update to our catalog will be made with the full spectrophotometric fitting of the entire sample using the NBURSTS+PHOT algorithm (Chilingarian & Katkov 2012) and resolving the star formation histories of about 10^5 galaxies with high-quality UV and NIR data.

We acknowledge the anonymous referee whose comments helped us to improve this manuscript. I.C.'s research is supported by the Smithsonian Astrophysical Observatory Telescope Data Center. I.Z. acknowledges the support by the Russian Scientific Foundation grant 14-50-00043 for the catalog assembly tasks and grant 14-12-00146 for the data publication and deployment system. The authors acknowledge partial support from the M.V. Lomonosov Moscow State University Program of Development, and a Russian–French PICS International Laboratory program (No. 6590) co-funded by the RFBR (project 15-52-15050), entitled "Galaxy Evolution Mechanisms in the Local Universe and at Intermediate Redshifts." The statistical studies of galaxy populations by I.C., I.Z., I.K., and E.R. are supported by the RFBR grant 15-32-21062 and the presidential grant MD-7355.2015.2. The authors are grateful to citizen scientists M. Chernyshov, A. Kilchik, A. Sergeev, R. Tihanovich, and A. Timirgazin for their valuable help with the development of the project website. In 2009–2011 the project was supported by the VO-Paris Data Centre and by the Action Specifique de l'Observatoire Virtuel (VO-France). Substantial progress in our project was achieved during our 2013, 2014, and 2015 annual Chamonix workshops and we are grateful to our host O. Bevan at Châlet des Sapins. This research has made use of TOPCAT, developed by Mark Taylor at the University of Bristol; Aladin, developed by the Centre de Données Astronomiques de Strasbourg (CDS); the "exploresdss" script by G. Mamon (IAP); and the VizieR catalog access tool (CDS). Funding for SDSS and SDSS-II has been provided by the Alfred P. Sloan Foundation, the participating institutions, the National Science Foundation, the U.S. Department of Energy, the National Aeronautics and Space Administration, the Japanese Monbukagakusho, the Max Planck Society, and the Higher Education Funding Council for England. The SDSS website is http://www.sdss.org/. *GALEX* (*Galaxy Evolution Explorer*) is a NASA Small Explorer, launched in April 2003. We gratefully acknowledge NASA's support in the construction, operation, and science analysis for the *GALEX* mission, developed in cooperation with the Centre National d'Etudes Spatiales of France and the Korean Ministry of Science and Technology.

[18] http://oirsa.cfa.harvard.edu/

Appendix A
Systematics in Emission Line Measurements Due to Stellar Population Template Mismatch

Absorption lines of the hydrogen Balmer series contain important information about stellar population ages (Worthey 1994): they become weaker when stars get older. At the same time, emission Balmer lines are used for ISM diagnostic and star formation studies (Baldwin et al. 1981). For the vast majority of galaxies in our sample, we see relatively weak emission lines on top of a stellar continuum. Therefore, in order to accurately measure emission line fluxes, we need to precisely model stellar populations. Hence, when gas emission lines reside on top of a stellar continuum, any systematic uncertainty in the modeling of absorption lines will affect emission line measurements. Specifically, the age mismatch in the stellar population fitting will substantially bias Balmer line fluxes.

In order to quantify this effect, we performed the following procedure: (i) we selected 2000 spectra from our sample with Balmer emission line intensities ranging from weak to strong based on their equivalent widths, (ii) we fitted those spectra using stellar population model grids fixing the SSP age to 2, 4, 8, and 16 Gyr, (iii) we measured emission line fluxes in the fitting residuals in these four sets of spectra, and (iv) we compared them to emission line fluxes obtained for the best-fitting stellar populations presented in our catalog.

In Figure 19 we present our results. It is clear that the age mismatch affects emission line fluxes for weak lines: the

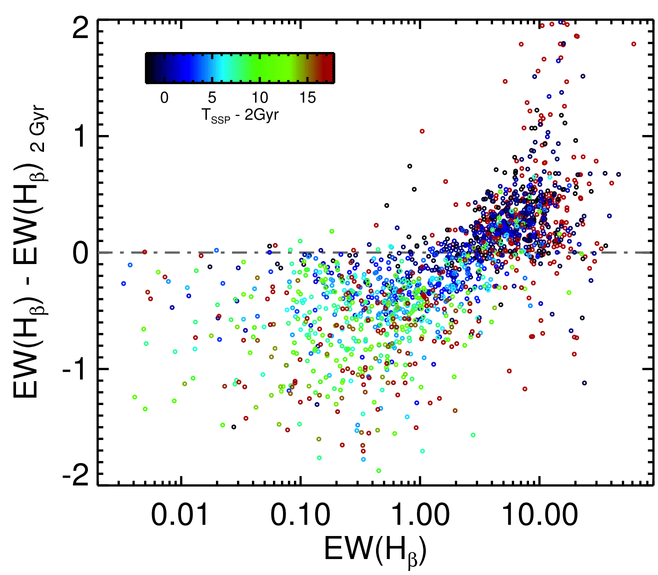

Figure 19. Stellar population age mismatch effect on Hβ flux measurements. The difference between the Hβ EW computed using the best-fitting SSP template and a template with the age fixed to 2 Gyr is plotted against the measured Hβ EW for the best-fitting SSP template. The age difference between the best-fitting SSP age and 2 Gyr is color-coded.

Table 4
Main Catalog Table (rcsed) Column Metadata and Descriptions

Column	Units	Datatype	UCD	Description
objid	⋯	bigint	meta.id;meta.main	SDSS ObjID (unique identifier)
specobjid	⋯	bigint	meta.id	SDSS SpecObjID (unique identifier within spectral galaxies sample)
mjd	⋯	integer	time.epoch	MJD of observation
plate	⋯	smallint	meta.id	SDSS plate ID
fiberid	⋯	smallint	meta.id	SDSS fiber ID
ra	deg	double	pos.eq.ra;meta.main	R.A. (J2000) of galaxy
dec	deg	double	pos.eq.dec;meta.main	Decl. (J2000) of galaxy
z	⋯	real	src.redshift	Galaxy redshift
zerr	⋯	real	stat.error;src.redshift	Uncertainty of galaxy redshift
zconf	⋯	real	stat.fit.param;src.redshift	SDSS redshift confidence
petror50_r	arcsec	real	phys.angSize	SDSS *r*adius containing 50% of Petrosian flux
e_bv	mag	real	phot.color.excess	$E(B-V)$ at this (l, b) from SFD98
specclass	⋯	smallint	src.spType	SDSS spectral classification
corrmag_fuv	mag	real	phot.mag;em.UV.FUV	Galactic extinction-corrected total (Kron-like elliptical aperture) magnitude in *GALEX* FUV filter
corrmag_nuv	mag	real	phot.mag;em.UV.NUV	Same as above for *GALEX* NUV filter
corrmag_u	mag	real	phot.mag;em.opt.U	Galactic extinction-corrected total (Petrosian) magnitude in SDSS *u* filter
corrmag_g	mag	real	phot.mag;em.opt.B	Same as above for SDSS *g* filter
corrmag_r	mag	real	phot.mag;em.opt.R	Same as above for SDSS *r* filter
corrmag_i	mag	real	phot.mag;em.opt.I	Same as above for SDSS *i* filter
corrmag_z	mag	real	phot.mag;em.opt.I	Same as above for SDSS *z* filter
corrmag_y	mag	real	phot.mag;em.IR.J	Same as above for UKIDSS *Y* filter
corrmag_j	mag	real	phot.mag;em.IR.J	Same as above for UKIDSS *J* filter
corrmag_h	mag	real	phot.mag;em.IR.H	Same as above for UKIDSS *H* filter
corrmag_k	mag	real	phot.mag;em.IR.K	Same as above for UKIDSS *K* filter
corrmag_fuv_err	mag	real	stat.error;phot.mag;em.UV.FUV	Uncertainty of corrmag_fuv column
corrmag_nuv_err	mag	real	stat.error;phot.mag;em.UV.NUV	Uncertainty of corrmag_nuv column
corrmag_u_err	mag	real	stat.error;phot.mag;em.opt.U	Uncertainty of corrmag_u column
corrmag_g_err	mag	real	stat.error;phot.mag;em.opt.B	Uncertainty of corrmag_g column
corrmag_r_err	mag	real	stat.error;phot.mag;em.opt.R	Uncertainty of corrmag_rcolumn
corrmag_i_err	mag	real	stat.error;phot.mag;em.opt.I	Uncertainty of corrmag_i column
corrmag_z_err	mag	real	stat.error;phot.mag;em.opt.I	Uncertainty of corrmag_z column
corrmag_y_err	mag	real	stat.error;phot.mag;em.IR.J	Uncertainty of corrmag_y column
corrmag_j_err	mag	real	stat.error;phot.mag;em.IR.J	Uncertainty of corrmag_j column
corrmag_h_err	mag	real	stat.error;phot.mag;em.IR.H	Uncertainty of corrmag_h column
corrmag_k_err	mag	real	stat.error;phot.mag;em.IR.K	Uncertainty of corrmag_k column
kcorr_fuv	mag	real	arith.factor;em.UV.FUV	K-correction for *GALEX* FUV magnitude
kcorr_nuv	mag	real	arith.factor;em.UV.NUV	Same as above for *GALEX* NUV magnitude
kcorr_u	mag	real	arith.factor;em.opt.U	K-correction for (Petrosian) SDSS *u* magnitude
kcorr_g	mag	real	arith.factor;em.opt.B	Same as above for SDSS *g* magnitude
kcorr_r	mag	real	arith.factor;em.opt.R	Same as above for SDSS *r* magnitude
kcorr_i	mag	real	arith.factor;em.opt.I	Same as above for SDSS *i* magnitude
kcorr_z	mag	real	arith.factor;em.opt.I	Same as above for SDSS *z* magnitude
kcorr_y	mag	real	arith.factor;em.IR.J	Same as above for UKIDSS *Y* magnitude
kcorr_j	mag	real	arith.factor;em.IR.J	Same as above for UKIDSS *J* magnitude
kcorr_h	mag	real	arith.factor;em.IR.H	Same as above for UKIDSS *H* magnitude
kcorr_k	mag	real	arith.factor;em.IR.K	Same as above for UKIDSS *K* magnitude
exp_radvel	km s^{-1}	real	spect.dopplerVeloc.opt	Radial velocity (exp SFH)
exp_radvel_err	km s^{-1}	real	stat.error;spect.dopplerVeloc.opt	Radial velocity error (exp SFH)
exp_veldisp	km s^{-1}	real	phys.veloc.dispersion	Velocity dispersion (exp SFH)
exp_veldisp_err	km s^{-1}	real	stat.error;phys.veloc.dispersion	Velocity dispersion error (exp SFH)
exp_tau	Myr	real	time.age	Age (exp SFH)
exp_tau_err	Myr	real	stat.error;time.age	Age error (exp SFH)
exp_met	⋯	real	phys.abund.Z	Metallicity (exp SFH)
exp_met_err	⋯	real	stat.error;phys.abund.Z	Metallicity error (exp SFH)
exp_chi2	⋯	real	stat.fit.chi2	Goodness of fit (exp SFH)
ssp_radvel	km s^{-1}	real	spect.dopplerVeloc.opt	Radial velocity (SSP)
ssp_radvel_err	km s^{-1}	real	stat.error;spect.dopplerVeloc.opt	Radial velocity error (SSP)
ssp_veldisp	km s^{-1}	real	phys.veloc.dispersion	Velocity dispersion (SSP)
ssp_veldisp_err	km s^{-1}	real	stat.error;phys.veloc.dispersion	Velocity dispersion error (SSP)
ssp_age	Myr	real	time.age	Age (SSP)
ssp_age_err	Myr	real	stat.error;time.age	Age error (SSP)
ssp_met	⋯	real	phys.abund.Z	Metallicity (SSP)
ssp_met_err	⋯	real	stat.error;phys.abund.Z	Metallicity error (SSP)
ssp_chi2	⋯	real	stat.fit.chi2	Goodness of fit (SSP)
zy_offset	mag	real	phot.mag;arith.diff	Offset applied to UKIDSS magnitudes to correct for mismatch with SDSS ones
spectrum_snr	⋯	real	stat.snr	Signal-to-noise ratio of SDSS spectrum at 5500A (restframe) in the 20A box

systematic errors grow when lines become weaker, and the difference between the best-fitting and fixed age templates gets higher. When ages are underestimated by the fitting procedure (i.e., a galaxy is older than the age of a template), Balmer emission line fluxes are underestimated, too. Because forbidden lines often used in the gas state diagnostics (e.g.,

Table 5
Fiber Magnitudes Table (`rcsed_fibermags`) Column Metadata and Descriptions

Column	Units	Datatype	UCD	Description
objid	···	bigint	meta.id;meta.main	SDSS ObjID (unique identifier)
corrfibmag_fuv	mag	real	phot.mag;em.UV.FUV	Galactic extinction-corrected $3''$ aperture magnitude in *GALEX* FUV filter
corrfibmag_nuv	mag	real	phot.mag;em.UV.NUV	Same as above for *GALEX* NUV filter
corrfibmag_u	mag	real	phot.mag;em.opt.U	Galactic extinction-corrected fiber ($3''$ aperture) magnitude in SDSS *u* filter
corrfibmag_g	mag	real	phot.mag;em.opt.B	Same as above for SDSS *g* filter
corrfibmag_r	mag	real	phot.mag;em.opt.R	Same as above for SDSS *r* filter
corrfibmag_i	mag	real	phot.mag;em.opt.I	Same as above for SDSS *i* filter
corrfibmag_z	mag	real	phot.mag;em.opt.I	Same as above for SDSS *z* filter
corrfibmag_y	mag	real	phot.mag;em.IR.J	Galactic extinction-corrected $3''$ aperture magnitude in UKIDSS *Y* filter
corrfibmag_j	mag	real	phot.mag;em.IR.J	Same as above for UKIDSS *J* filter
corrfibmag_h	mag	real	phot.mag;em.IR.H	Same as above for UKIDSS *H* filter
corrfibmag_k	mag	real	phot.mag;em.IR.K	Same as above for UKIDSS *K* filter
corrfibmag_fuv_err	mag	real	stat.error;phot.mag;em.UV.FUV	Uncertainty of corrfibmag_fuv column
corrfibmag_nuv_err	mag	real	stat.error;phot.mag;em.UV.NUV	Uncertainty of corrfibmag_nuv column
corrfibmag_u_err	mag	real	stat.error;phot.mag;em.opt.U	Uncertainty of corrfibmag_u
corrfibmag_g_err	mag	real	stat.error;phot.mag;em.opt.B	Uncertainty of corrfibmag_g
corrfibmag_r_err	mag	real	stat.error;phot.mag;em.opt.R	Uncertainty of corrfibmag_r
corrfibmag_i_err	mag	real	stat.error;phot.mag;em.opt.I	Uncertainty of corrfibmag_i
corrfibmag_z_err	mag	real	stat.error;phot.mag;em.opt.I	Uncertainty of corrfibmag_z
corrfibmag_y_err	mag	real	stat.error;phot.mag;em.IR.J	Uncertainty of corrfibmag_y
corrfibmag_j_err	mag	real	stat.error;phot.mag;em.IR.J	Uncertainty of corrfibmag_j
corrfibmag_h_err	mag	real	stat.error;phot.mag;em.IR.H	Uncertainty of corrfibmag_h
corrfibmag_k_err	mag	real	stat.error;phot.mag;em.IR.K	Uncertainty of corrfibmag_k
kcorrfib_fuv	mag	real	arith.factor;em.UV.FUV	K-correction for $3''$ aperture *GALEX* FUV magnitude
kcorrfib_nuv	mag	real	arith.factor;em.UV.NUV	Same as above for *GALEX* NUV magnitude
kcorrfib_u	mag	real	arith.factor;em.opt.U	K-correction for fiber ($3''$ aperture) SDSS *u* magnitude
kcorrfib_g	mag	real	arith.factor;em.opt.B	Same as above for SDSS *g* magnitude
kcorrfib_r	mag	real	arith.factor;em.opt.R	Same as above for SDSS *r* magnitude
kcorrfib_i	mag	real	arith.factor;em.opt.I	Same as above for SDSS *i* magnitude
kcorrfib_z	mag	real	arith.factor;em.opt.I	Same as above for SDSS *z* magnitude
kcorrfib_y	mag	real	arith.factor;em.IR.J	K-correction for $3''$ aperture UKIDSS *Y* magnitude
kcorrfib_j	mag	real	arith.factor;em.IR.J	Same as above for UKIDSS *J* magnitude
kcorrfib_h	mag	real	arith.factor;em.IR.H	Same as above for UKIDSS *H* magnitude
kcorrfib_k	mag	real	arith.factor;em.IR.K	Same as above for UKIDSS *K* magnitude

[N II] or [O III]) do not lie on top of strong age-sensitive absorption features, their fluxes remain virtually unaffected, hence moving a galaxy over the diagnostic plots (e.g., BPT) and potentially leading to the ionization mechanism misclassification.

Appendix B
Catalog Compilation: Sql Query

To select the core sample of galaxies, we performed the following SQL query in the SDSS CasJobs service in the DR7 context (see details in Section 2.1):

```
SELECT
 p.objID, p.ra, p.dec,

 p.modelMag_u, p.modelMagErr_u, p.modelMag_g, p.
  modelMagErr_g,
 p.modelMag_r, p.modelMagErr_r, p.modelMag_i, p.
  modelMagErr_i,
 p.modelMag_z, p.modelMagErr_z,

 petroMag_u, petroMagErr_u, petroMag_g, petroMagErr_g,
 petroMag_r, petroMagErr_r, petroMag_i, petroMagErr_i,
 petroMag_z, petroMagErr_z,

 p.fiberMag_u, p.fiberMagErr_u, p.fiberMag_g, p.
  fiberMagErr_g,
```

(Continued)

```
 p.fiberMag_r, p.fiberMagErr_r, p.fiberMag_i, p.
  fiberMagErr_i,
 p.fiberMag_z, p.fiberMagErr_z,

 p.petroR50_u, p.petroR50Err_u, p.petroR50_g, p.
  petroR50Err_g,
 p.petroR50_r, p.petroR50Err_r, p.petroR50_i, p.
  petroR50Err_i,
 p.petroR50_z, p.petroR50Err_z,

 p.extinction_u, p.extinction_g, p.extinction_r, p.
  extinction_i, p.extinction_z,

 s.specObjID, s.mjd, s.plate, s.fiberID,
 s.z, s.zerr, s.zconf, s.objType, s.sn_0, s.sn_1, s.sn_2,
 (SELECT stripe FROM dbo.fCoordsFromEq(p.ra,p.dec)) AS
  stripe,
 s.specClass

INTO mydb.RCSED_SDSS
FROM PhotoObj AS p, SpecObj as s
WHERE
 s.bestObjid = p.objID
 AND s.z > = 0.007
 AND s.z <0.6
 AND s.specClass IN (dbo.fSpecClass('GAL_EM'), dbo.
  fSpecClass('GALAXY'))
```

Table 6
Gas Phase Metallicity Table (`rcsed_gasmet`) Column Metadata and Descriptions

Column	Units	Datatype	UCD	Description
id	⋯	bigint	meta.id;meta.main	Primary key
objid	⋯	bigint	⋯	SDSS ObjID
mjd	days	integer	time.epoch	MJD of observation
plate	⋯	smallint	meta.id	SDSS plate ID
fiberid	⋯	smallint	meta.id	SDSS fiber ID
e_bv	mag	real	phot.color.excess	Intrinsic $E(B-V)$
gas_oh_d16	⋯	real	phys.abund.Z	Oxygen abundance of ionized gas (12 + log O/H) calculated using Dopita+16 calibration from Gaussian fit to emission lines
gas_oh_d16_err	⋯	real	phys.abund.Z	Error of oxygen abundance of ionized gas (12 + log O/H) calculated using Dopita+16 calibration from Gaussian fit to emission lines
gas_oh_izi	⋯	real	phys.abund.Z	Oxygen abundance of ionized gas (12 + log O/H) calculated using IZI calibration from Gaussian fit to emission lines
gas_oh_izi_errlo	⋯	real	stat.error;phys.abund.Z	Lower error of oxygen abundance of ionized gas (12 + log O/H) calculated using IZI calibration from Gaussian fit to emission lines
gas_oh_izi_errhi	⋯	real	stat.error;phys.abund.Z	Upper error of oxygen abundance of ionized gas (12 + log O/H) calculated using IZI calibration from Gaussian fit to emission lines
q_izi	⋯	real	phys.ionizParam.rad	Ionization parameter calculated using IZI calibration from Gaussian fit to emission lines
q_izi_errlo	⋯	real	stat.error;phys.ionizParam.rad	Lower error of ionization parameter calculated using IZI calibration from Gaussian fit to emission lines
q_izi_errhi	⋯	real	stat.error;phys.ionizParam.rad	Upper error of ionization parameter calculated using IZI calibration from Gaussian fit to emission lines

Table 7
Gaussian Fit to Emission Lines Table (`rcsed_lines_gauss`) Column Metadata and Descriptions

Column	Units	Datatype	UCD	Description
id	⋯	bigint	meta.id; meta.main	Primary key
objid	⋯	bigint	meta.id	SDSS ObjID
mjd	days	integer	time.epoch	MJD of observation
plate	⋯	smallint	meta.id	SDSS plate ID
fiberid	⋯	smallint	meta.id	SDSS fiber ID
forbid_v	km s^{-1}	real	phys.veloc	Velocity measured simultaneously in all forbidden lines
forbid_v_err	km s^{-1}	real	stat.error; phys.veloc	Uncertainty in the velocity measured simultaneously in all forbidden lines
forbid_sig	km s^{-1}	real	phys.veloc.dispersion	Velocity dispersion measured simultaneously in all forbidden lines
forbid_sig_err	km s^{-1}	real	stat.error; phys.veloc.dispersion	Uncertainty in the velocity dispersion measured simultaneously in all forbidden lines
allowed_v	km s^{-1}	real	phys.veloc	Velocity measured simultaneously in all allowed lines
allowed_v_err	km s^{-1}	real	stat.error; phys.veloc	Uncertainty in the velocity measured simultaneously in all allowed lines
allowed_sig	km s^{-1}	real	phys.veloc.dispersion	Velocity dispersion measured simultaneously in all allowed lines
allowed_sig_err	km s^{-1}	real	stat.error; phys.veloc.dispersion	Uncertainty in the velocity dispersion measured simultaneously in all allowed lines
chi2	⋯	real	stat.fit.chi2	Reduced goodness of fit
f3727_oii_flx	10^{-17} erg s^{-1} cm^{-2}	real	phot.flux; spect.line	Flux from Gaussian fit to continuum subtracted data of [O II] (3727 Å) line
f3727_oii_flx_err	10^{-17} erg s^{-1} cm^{-2}	real	stat.error; phot.flux; spect.line	Uncertainty in the flux from Gaussian fit to continuum subtracted data of [O II] (3727 Å) line
f3727_oii_cnt	10^{-17} erg s^{-1} cm^{-2}/Å	real	phot.flux.density; spect.continuum	Continuum level at [O II] (3727 Å) line center
f3727_oii_cnt_err	10^{-17} erg s^{-1} cm^{-2}/Å	real	stat.error; phot.flux.density; spect.continuum	Uncertainty in the continuum level at [O II] (3727 Å) line center
f3727_oii_ew	Å	real	spect.line.eqWidth	Equivalent width from Gaussian fit to continuum subtracted data of [O II] (3727 Å) line
f3727_oii_ew_err	Å	real	stat.error; spect.line.eqWidth	Uncertainty in the equivalent width from Gaussian fit to continuum subtracted data of [O II] (3727 Å) line

Table 8
Non-parametric Fit to Emission Lines Table (`rcsed_lines_nonpar`) Column Metadata and Descriptions

Column	Units	Datatype	UCD	Description
id	...	bigint	meta.id; meta.main	Primary key
objid	...	bigint	meta.id	SDSS ObjID
mjd	days	integer	time.epoch	MJD of observation
plate	...	smallint	meta.id	SDSS plate ID
fiberid	...	smallint	meta.id	SDSS fiber ID
forbid_v	km s^{-1}	real	phys.veloc	Velocity measured simultaneously in all forbidden lines
forbid_sig	km s^{-1}	real	phys.veloc.dispersion	Velocity dispersion measured simultaneously in all forbidden lines
allowed_v	km s^{-1}	real	phys.veloc	Velocity measured simultaneously in all allowed lines
allowed_sig	km s^{-1}	real	phys.veloc.dispersion	Velocity dispersion measured simultaneously in all allowed lines
chi2	...	real	stat.fit.chi2	Reduced goodness of fit
f3727_oii_flx	10^{-17} erg s^{-1} cm^{-2}	real	phot.flux; spect.line	Flux from non-parametric fit to continuum subtracted data of [O II] (3727 Å) line
f3727_oii_flx_err	10^{-17} erg s^{-1} cm^{-2}	real	stat.error; phot.flux; spect.line	Uncertainty in the flux from non-parametric fit to continuum subtracted data of [O II] (3727 Å) line
f3727_oii_cnt	10^{-17} erg s^{-1} cm^{-2}/Å	real	phot.flux.density; spect.continuum	Continuum level at [O II] (3727 Å) line center
f3727_oii_cnt_err	10^{-17} erg s^{-1} cm^{-2}/Å	real	stat.error; phot.flux.density; spect.continuum	Uncertainty in the continuum level at [O II] (3727 Å) line center
f3727_oii_ew	Å	real	spect.line.eqWidth	Equivalent width from non-parametric fit to continuum subtracted data of [O II] (3727 Å) line
f3727_oii_ew_err	Å	real	stat.error; spect.line.eqWidth	Uncertainty in the equivalent width from non-parametric fit to continuum subtracted data of [O II] (3727 Å) line

This query returned 800,311 rows with 12 duplicate objects for which the SDSS `SpecObj` table contains two records, despite it being documented to be clean from duplicates. We discard these duplicate spectra by keeping the record with the higher S/N from each pair of duplicates (and hence having, e.g., better redshift estimate). For now we continue with the sample of 800,299 galaxies.

The coordinates of the obtained galaxies were then uploaded to the *GALEX* CasJobs service and the following query was performed there in the GALEXGR6Plus7 context:

```
SELECT
 sdss.objid,
 galex_objid,

 nuv_mag, nuv_magerr, fuv_mag, fuv_magerr,
 nuv_mag_aper_1, nuv_magerr_aper_1, nuv_mag_auto,
 fuv_mag_aper_1, fuv_magerr_aper_1, fuv_mag_auto,
 e_bv
INTO mydb.RCSED_SDSS_GALEX

FROM
 (
  SELECT
   s.objid,
   (SELECT objid FROM dbo.fGetNearestObjEq(s.ra, s.dec,
  0.05)) AS galex_objid
  FROM
   mydb.RCSED_SDSS_coords AS s
 ) AS sdss
JOIN
 photoObjAll AS p
 ON sdss.galex_objid = p.objid
```

This query returned 485,996 rows.

Appendix C
Catalog Column Descriptions

In Tables 4–8 we provide descriptions and metadata for the columns of the original tables of RCSED, which are shown in blue in Figure 18. The external data sets available in the RCSED database are described in the corresponding original papers (see the text for references).

This column information is identical to the FITS tables distribution of the catalog, as well as when accessing the RCSED database through the Table Access Protocol, or using the catalog website http://rcsed.sai.msu.ru. For each column name in every table we give (i) units (dash indicates that a column is dimensionless or units are not applicable to it), (ii) data type in the database convention in order to guide a user on the precision and purpose of a column, (iii) IVOA Unified Content Descriptor (UCD) that helps one to identify equivalent physical quantities available for comparison in the VO or to associate a column and its uncertainty, and (iv) human-readable description of the column contents. When a table includes many similar columns as in the case of the spectral line properties in the `rcsed_lines_gauss` and `rcsed_lines_nonpar` database tables, we only give the metadata for the first group of columns in it and abridge the rest (Tables 7 and 8). The complete list of emission lines included in our catalog and the column name prefixes in `rcsed_lines_gauss` and `rcsed_lines_nonpar` are given in Table 2.

References

Q4

Abazajian, K. N., Adelman-McCarthy, J. K., Agüeros, M. A., et al. 2009, ApJS, 182, 543
Andrews, B. H., & Martini, P. 2013, ApJ, 765, 140
Baldwin, J. A., Phillips, M. M., & Terlevich, R. 1981, PASP, 93, 5
Becker, R. H., White, R. L., & Helfand, D. J. 1995, ApJ, 450, 559
Bernardi, M., Sheth, R. K., Annis, J., et al. 2003, AJ, 125, 1849
Blanc, G. A., Kewley, L., Vogt, F. P. A., & Dopita, M. A. 2015, ApJ, 798, 99
Blanton, M. R., Hogg, D. W., Bahcall, N. A., et al. 2003, ApJ, 592, 819

Blanton, M. R., Schlegel, D. J., Strauss, M. A., et al. 2005, AJ, 129, 2562
Brinchmann, J., Charlot, S., White, S. D. M., et al. 2004, MNRAS, 351, 1151
Bruzual, G., & Charlot, S. 2003, MNRAS, 344, 1000
Cappellari, M., Bacon, R., Bureau, M., et al. 2006, MNRAS, 366, 1126
Cappellari, M., & Emsellem, E. 2004, PASP, 116, 138
Chilingarian, I., Prugniel, P., Sil'chenko, O., & Koleva, M. 2007a, in IAU Symp. 241, Stellar Populations as Building Blocks of Galaxies, ed. A. Vazdekis & R. R. Peletier (Cambridge: Cambridge Univ. Press), 175 arXiv:0709.3047
Chilingarian, I., & Zolotukhin, I. 2015, Sci, 348, 418
Chilingarian, I. V. 2009, MNRAS, 394, 1229
Chilingarian, I. V., Cayatte, V., Durret, F., et al. 2008, A&A, 486, 85
Chilingarian, I. V., & Katkov, I. Y. 2012, in IAU Symp. 284, The Spectral Energy Distribution of Galaxies—SED 2011, ed. R. J. Tuffs & C. C. Popescu 26 Q5
Chilingarian, I. V., Melchior, A.-L., & Zolotukhin, I. Y. 2010, MNRAS, 405, 1409
Chilingarian, I. V., Prugniel, P., Sil'chenko, O. K., & Afanasiev, V. L. 2007b, MNRAS, 376, 1033
Chilingarian, I. V., & Zolotukhin, I. Y. 2012, MNRAS, 419, 1727
Cid Fernandes, R., Stasińska, G., Schlickmann, M. S., et al. 2010, MNRAS, 403, 1036
Colless, M., Dalton, G., Maddox, S., et al. 2001, MNRAS, 328, 1039
Damjanov, I., Chilingarian, I., Hwang, H. S., & Geller, M. J. 2013, ApJL, 775, L48
Damjanov, I., Hwang, H. S., Geller, M. J., & Chilingarian, I. 2014, ApJ, 793, 39
de Vaucouleurs, G., de Vaucouleurs, A., Corwin, H. G., Jr., et al. 1991, Third Reference Catalogue of Bright Galaxies. Volume I: Explanations and references. Volume II: Data for galaxies between 0^h and 12^h. Volume III: Data for galaxies between 12^h and 24^h
Djorgovski, S., & Davis, M. 1987, ApJ, 313, 59
Dopita, M. A., Kewley, L. J., Sutherland, R. S., & Nicholls, D. C. 2016, Ap&SS, 361, 61
Dopita, M. A., Sutherland, R. S., Nicholls, D. C., Kewley, L. J., & Vogt, F. P. A. 2013, ApJS, 208, 10
Faber, S. M., & Jackson, R. E. 1976, ApJ, 204, 668
Fabricant, D., Chilingarian, I., Hwang, H. S., et al. 2013, PASP, 125, 1362
Fabricant, D., Fata, R., Roll, J., et al. 2005, PASP, 117, 1411
Fukugita, M., Nakamura, O., Okamura, S., et al. 2007, AJ, 134, 579
Fukugita, M., Shimasaku, K., & Ichikawa, T. 1995, PASP, 107, 945
Gallazzi, A., Charlot, S., Brinchmann, J., & White, S. D. M. 2006, MNRAS, 370, 1106
Groves, B., Brinchmann, J., & Walcher, C. J. 2012, MNRAS, 419, 1402
Hewett, P. C., Warren, S. J., Leggett, S. K., & Hodgkin, S. T. 2006, MNRAS, 367, 454
Hinshaw, G., Larson, D., Komatsu, E., et al. 2013, ApJS, 208, 19
Kauffmann, G., Heckman, T. M., White, S. D. M., et al. 2003, MNRAS, 341, 33
Kewley, L. J., & Ellison, S. L. 2008, ApJ, 681, 1183
Kewley, L. J., Groves, B., Kauffmann, G., & Heckman, T. 2006, MNRAS, 372, 961
Lawrence, A., Warren, S. J., Almaini, O., et al. 2007, MNRAS, 379, 1599
Lawson, C. L., & Hanson, R. J. 1995, Classics in Applied Mathematics, Vol. 15, Solving Least Squares Problems (Philadelphia: SIAM)
Le Borgne, D., Rocca-Volmerange, B., Prugniel, P., et al. 2004, A&A, 425, 881
Lintott, C., Schawinski, K., Bamford, S., et al. 2011, MNRAS, 410, 166
Lintott, C. J., Schawinski, K., Slosar, A., et al. 2008, MNRAS, 389, 1179
López-Sánchez, Á. R., Dopita, M. A., Kewley, L. J., et al. 2012, MNRAS, 426, 2630
Markwardt, C. B. 2009, in ASP Conf. Ser. 411, Astronomical Data Analysis Software and Systems XVIII, ed. D. A. Bohlender, D. Durand, & P. Dowler (San Francisco, CA: ASP), 251
Martin, D. C., Fanson, J., Schiminovich, D., et al. 2005, ApJL, 619, L1
Matković, A., & Guzmán, R. 2005, MNRAS, 362, 289
Matteucci, F. 1994, A&A, 288, 57
Newman, J. A., Cooper, M. C., Davis, M., et al. 2013, ApJS, 208, 5
Oh, K., Sarzi, M., Schawinski, K., & Yi, S. K. 2011, ApJS, 195, 13
Oh, K., Yi, S. K., Schawinski, K., et al. 2015, ApJS, 219, 1
Petrosian, V. 1976, ApJL, 209, L1
Prugniel, P., & Soubiran, C. 2004, arXiv:astro-ph/0409214
Prugniel, P., Soubiran, C., Koleva, M., & Le Borgne, D. 2007, arXiv:astro-ph/0703658
Sánchez-Blázquez, P., Peletier, R. F., Jiménez-Vicente, J., et al. 2006, MNRAS, 371, 703
Saulder, C., Mieske, S., Zeilinger, W. W., & Chilingarian, I. 2013, A&A, 557, A21
Saulder, C., van Kampen, E., Chilingarian, I., Mieske, S., & Zeilinger, W. W. 2016, A&A, 596, A14
Saunders, W., Sutherland, W. J., Maddox, S. J., et al. 2000, MNRAS, 317, 55
Schechter, P. 1976, ApJ, 203, 297
Schlegel, D. J., Finkbeiner, D. P., & Davis, M. 1998, ApJ, 500, 525
Serra, P., & Trager, S. C. 2007, MNRAS, 374, 769
Simard, L., Mendel, J. T., Patton, D. R., Ellison, S. L., & McConnachie, A. W. 2011, ApJS, 196, 11
Skrutskie, M. F., Cutri, R. M., Stiening, R., et al. 2006, AJ, 131, 1163
Taylor, M. B. 2005, in ASP Conf. Ser. 347, Astronomical Data Analysis Software and Systems XIV, ed. P. Shopbell, M. Britton, & R. Ebert (San Francisco, CA: ASP), 29
Taylor, M. B. 2006, in ASP Conf. Ser. 351, Astronomical Data Analysis Software and Systems XV, ed. C. Gabriel et al. (San Francisco, CA: ASP), 666
Tremonti, C. A., Heckman, T. M., Kauffmann, G., et al. 2004, ApJ, 613, 898
Vazdekis, A., Sánchez-Blázquez, P., Falcón-Barroso, J., et al. 2010, MNRAS, 404, 1639
Worthey, G. 1994, ApJS, 95, 107
Wright, E. L., Eisenhardt, P. R. M., Mainzer, A. K., et al. 2010, AJ, 140, 1868
Yasuda, N., Fukugita, M., Narayanan, V. K., et al. 2001, AJ, 122, 1104
Yates, R. M., Kauffmann, G., & Guo, Q. 2012, MNRAS, 422, 215
Zahid, H. J., Baeza Hochmuth, N., Geller, M. J., et al. 2016, ApJ, 831, 146
Zahid, H. J., Damjanov, I., Geller, M. J., & Chilingarian, I. 2015, ApJ, 806, 122